5-2013

An Investigation of Rare Earth Co-doping in Fluorochlorozirconate Glass-Ceramic Imaging Plates to Improve the Storage Phosphor Properties for Computed Radiography

Sharon Gray
sgray22@utk.edu

To the Graduate Council:

I am submitting herewith a thesis written by Sharon Gray entitled "An Investigation of Rare Earth Co-doping in Fluorochlorozirconate Glass-Ceramic Imaging Plates to Improve the Storage Phosphor Properties for Computed Radiography." I have examined the final electronic copy of this thesis for form and content and recommend that it be accepted in partial fulfillment of the requirements for the degree of Master of Science, with a major in Biomedical Engineering.

Jacqueline A. Johnson, Major Professor

We have read this thesis and recommend its acceptance:

Charles E. Johnson, Lino Costa

Accepted for the Council:
Carolyn R. Hodges

Vice Provost and Dean of the Graduate School

(Original signatures are on file with official student records.)

An Investigation of Rare Earth Co-doping in Fluorochlorozirconate Glass-Ceramic Imaging Plates to Improve the Storage Phosphor Properties for Computed Radiography

A Thesis Presented for the
Master of Science
Degree
The University of Tennessee, Knoxville

Sharon Gray
May 2013

DEDICATION

This endeavor is dedicated to my family, especially my grandmothers.

ACKNOWLEDGEMENTS

I wish to express sincere gratitude to my advisor, Dr. Jacqueline Johnson, and my committee members, Dr. Charles Johnson and Dr. Lino Costa, for providing this unique and rewarding learning experience. I want to give special thanks to Drs. Johnson for their graciousness.

Several people performed critical roles in this research. Kathleen Lansford, Alexander Terekhov, and Doug Warnberg provided technical assistance. X-ray diffraction experiments were performed at Vanderbilt University with assistance of Jeremy Beam and Dr. Charles Lukehart. Dr. Rick Lubinsky (State University of New York, Stony Brook) performed the photostimulated luminescence experiments.

I want to thank all the students, summer interns, faculty, and staff at UTSI for making my time here so memorable. Friends, Sabrina Hurlock and Coral Franklin kept me grounded. I especially appreciate friendships developed with Jason Hah, Chris Foerster, Christian Paßlick and Charlotte Pfau.

In particular, I want to acknowledge my colleague and friend, Lee Leonard, who always provided invaluable input during every step of my UTSI experience, both in the classroom and in the lab. The patience, work ethic, and humor made interaction a pure pleasure in every way.

Financial support was provided by the following grants for which I am grateful.
National Science Foundation (Grant Number DMR1001381)
National Institutes of Health (Grant Number 5R01EB006145)
National Institute of Biomedical Imaging and Bioengineering

ABSTRACT

Computed radiography is a standard medical imaging technology that uses photostimulable storage phosphor imaging plates to create an image. X-rays create electron hole pairs within the plate which recombine upon stimulation by a laser, producing light which is read out and stored as a digital image. Modern imaging plates contain an active layer of crystalline storage phosphors embedded in a polymer binder. The resolution of images from these plates is reduced due to light scattering at grain boundaries during readout. Fluorochlorozirconate (FCZ) glass-ceramic imaging plates containing $BaCl_2$:Eu^{2+} [barium chloride] [europium] nanocrystals in the orthorhombic phase have been developed to decrease light scattering during readout and improve resolution for applications such as mammography where a high level of detail is required. However, these plates lack the conversion efficiency (CE) of current plates and therefore require a higher x-ray dose to provide sufficient light to produce an image. This work investigates the use of co-doping to increase the CE of FCZ glass-ceramic imaging plates.

A series of fluorochlorozirconate (FCZ) glass samples were produced, replacing the $EuCl_2$ with HoF_3 [holmium] to determine the effects of co-doping on light output. The samples were characterized using differential scanning calorimetry to determine the temperature at which orthorhombic $BaCl_2$ crystallization occurs. Thermal treatments were performed to precipitate $BaCl_2$ nanocrystals in the orthorhombic phase, creating a glass ceramic. The heat treated samples were characterized using phosphorimetry and x-ray diffraction to confirm the crystalline phases present. Photostimulated luminescence (PSL) experiments were conducted to evaluate light output. The results indicate that the addition of HoF_3 increases the CE even though HoF_3 singly doped FCZ glass ceramics do not exhibit any PSL.
In an effort to reduce the costs of the FCZ glass-ceramic imaging plates, experiments were conducted to see if less costly $EuCl_3$ could be reduced to form the more expensive $EuCl_2$ through heating in an inert atmosphere. Three different heating profiles were tested. The percent conversion was evaluated using Mössbauer [Mossbauer] spectroscopy. The results show that $EuCl_2$ can be successfully synthesized from $EuCl_3$.

TABLE OF CONTENTS

LIST OF TABLES

LIST OF FIGURES

CHAPTER 1

INTRODUCTION & BACKGROUND

Computed Radiography

Computed radiography (CR) is one of the medical imaging diagnostic technologies currently being used. Traditional screen film (SF) radiography systems are being replaced by computed radiography (CR) and digital radiography (DR) which uses either direct or indirect detection. Each imaging system is distinguished by the detection medium, the way the image is stored/recorded within the medium, and how the stored image is retrieved. During x-ray irradiation, SF systems store the image on film which must be chemically processed to retrieve the image. In CR imaging systems, upon irradiation, a photostimulable storage phosphor plate stores the latent image in electron hole traps until they recombine under laser stimulation, emitting photons that are converted to a digital image. DR indirect conversion uses a flat panel screen with scintillator material that converts X-rays to visible light photons upon irradiation. Visible light is converted to electrical charge. The image is stored as electrical charge which is converted to a digital x-ray image. DR direct conversion uses a flat panel with photoconductor material to produce electrical charges directly from the x-rays upon irradiation [1].

Each of the radiographic imaging system offers advantages and disadvantages over the alternatives. The CR and DR systems both produce digital images which may be enhanced or manipulated with algorithms to remove artifacts. Produced images may be transmitted electronically to other locations or archived. The SF system produces a hard copy, which requires storage space and is tedious to transport from location to location. The CR system offers more cross table image capture flexibility than DR systems which use a flat panel screen detector embedded in a bucky table or bucky wall. The storage phosphor imaging plates used in CR are erased and reused which should reduce the cost to patients. DR systems produce an image more rapidly than the SF and CR systems requiring cassette processing, but the equipment cost makes DR the most expensive method of radiography.

Computed Radiography Imaging Plates

Computed radiography systems use imaging plates made of photostimulated luminescence materials. The portable plates are encased in cassettes. The cassette material is opaque to visible light, but transparent to x-ray radiation. After exposure, the plate is removed to a central processing system where the plate is removed from the cassette in darkness. It is raster scanned with a laser to release the stored latent image. As the laser sweeps the plate pixel by pixel and line by line, the emitted light is collected and detected with a photomultiplier tube whose output signal is amplified and digitized to form the radiographic image. Any residual image remaining in the plate is erased by exposure to white light. The plate is reinserted into the cassette and is ready for re-use as an unexposed image plate. A schematic of the process is shown in Figure 1.

Current CR storage phosphor plates consist of a support substrate layer and a layer containing x-ray storage phosphor crystallites embedded in an organic binder. Upon X-ray irradiation, complementary defects (electron hole pairs) are generated in the crystallites. The absorbed x-ray energy is stored in these defects. The energy is trapped as the latent image. The laser stimulation provides the electron with sufficient energy to recombine with the hole. The recombination energy is transferred to the luminescent center which emits a characteristic photon. This process is termed photostimulated luminescence (PSL). [2]

Storage phosphor plates currently being used experience loss of resolution due to diffraction and scattering during the readout process when stimulating radiation interacts with the polycrystallites dispersed in the polymer binder [3]. Soft tissue imaging for diagnostic mammography requires a high level of spatial resolution. A fluorochlorozirconate glass (FCZ) has been developed which has superior spatial resolution [4, 5]. The scattering due to the polymer binder is eliminated since the nanocrystals are embedded in a glass matrix. However, FCZ lacks the PSL conversion efficiency of the current imaging plates.

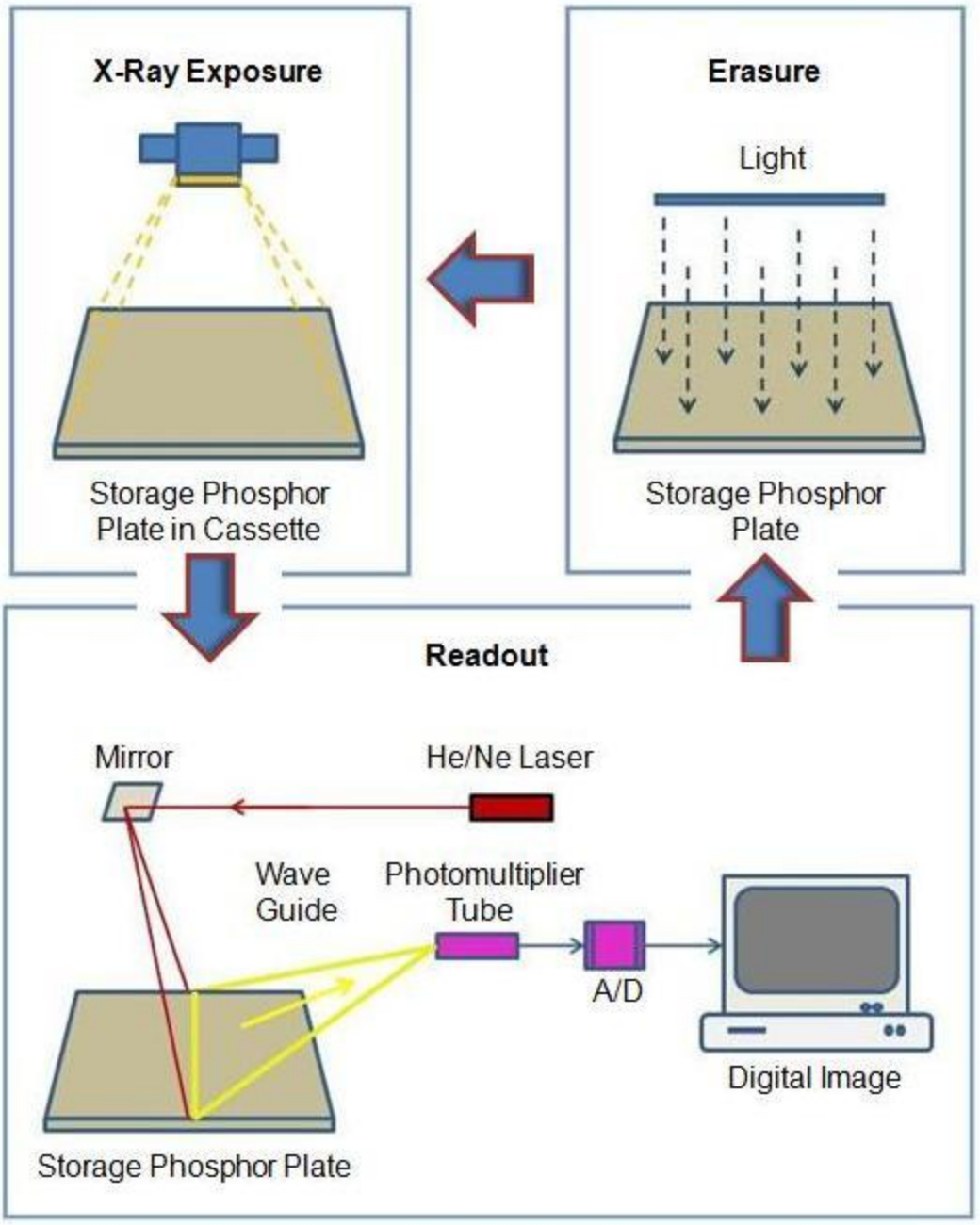

Figure 1. Exposure, Readout, and Erasure of Storage Phosphor Plate used in Computed Radiography

Fluorochlorozirconate Glass

Fluorozirconate glass was discovered in 1975 by Poulain, Poulain and Lucas in Rennes, France. Containing 50% ZrF_4, 25% BaF_2, and 25% NaF [6] the glass system joined other heavy metal fluoride glasses (HMFGs) including fluoroaluminate, fluorogallate, fluorindiate, fluoromanganate, and fluoroscandate glasses. The classification name is based on the primary constituent component in the fluorine and metals glass system [7].

Fluorozirconate glasses have been continually developed. Standard compositions are modified by incorporating selected chemicals to achieve specific glass properties. This has led to new fluorozirconate glass forming systems, including ZBLAN (ZrF_4-BaF_2-LaF_3-AlF_3-NaF) by Poulain and Lucas at the University of Rennes. The addition of AlF_3 and LaF_3 was found to increase glass stability [7, 8, 9, 10]. The separation between the glass transition temperature (T_g) and the crystallization temperature (T_x) is an indicator of viscosity and is used as a criterion for stability assessment.

ZBLAN became the most heavily studied HMFG. It was considered to be the most stable HMFG and an excellent host for rare earth ions [11]. Uses include optical fibers and photovoltaics. ZBLAN doped with rare earth ions has been a material of interest in creating a better storage phosphor plate [4, 12, 13,14,15, 16] due to its low phonon energy [16, 17, 18,19,20] and because thermal treatments determine the nanocrystal phase that precipitates during the crystallization process [19, 20]. Low phonon energy reduces non-radiative energy losses.

The developed fluorochlorozirconate glass ((ZrF_4-$BaCl_2$-LaF_3-AlF_3-NaF) is a modified ZBLAN in which BaF_2 is replaced with $BaCl_2$. The addition of chlorine ions enables the nucleation of $BaCl_2$ phase specific nanocrystals during a thermal treatment process [21]. Inclusion of $EuCl_2$ and InF_3 enhance the glass ceramic properties.

The rare earth dopant $EuCl_2$ is added to enhance the luminescent properties. While $EuCl_2$ embedded in the glass matrix does not fluoresce, when $EuCl_2$ associates with the $BaCl_2$ nanocrystals during thermal treatment, $EuCl_2$ fluorescence does occur [22, 23]. $BaCl_2$:Eu^{2+} nanocrystals in the orthorhombic phase are required to produce a storage phosphor. $BaCl_2$:Eu^{3+} nanocrystals do not produce electron hole pair defects required for photostimulated luminescence [24, 25, 26]. EuF_2 as a dopant has been investigated, but the phase transition from hexagonal to orthorhombic structure occurs at a higher temperature [14].

ZrF_4 is the primary component in ZBLAN, usually making up about 50 percent of the composition. When it reduces to ZrF_3, black specks precipitate in the glass

ceramic, diminishing the quality of the glass. Inclusion of InF_3 limits the effect by acting as an oxidizer. When ZrF_4 reduces to ZrF_3, InF_3 reduces to InF and the ZrF_3 oxidizes back to ZrF_4 [14, 27]. It has been shown that InF_3 is a critical component for orthorhombic crystallization to occur during heat treatments [28].

Rare Earth Doping

The luminescent properties of singly doped and co-doped fluorozirconate glasses have been investigated. Ho^{3+} has been shown to exhibit multiphoton processes including excited state absorption, energy transfer upconversion, photon avalanche absorption and downconversion [29, 30, 31, 32, 33, 34, 35, 36].

Impurities which lead to nanocrystal defects (electron hole pairs) and influence PSL properties are introduced by rare earth doping [15]. To optimize the storage phosphor material for radiographic imaging plates, we investigate the impact of co-doping with HoF_3 on conversion efficiency or light output.

Inclusion of a rare earth dopant like $EuCl_2$ is a critical ingredient in FCZ if an efficient storage phosphor is to be produced. However, due to limited quantities, $EuCl_2$ is the most expensive component of FCZ glass. In an effort to address environmental issues, the amount of europium production has been significantly reduced, and the trend is expected to continue. As a raw material, Eu^{3+}, which is the stable state, is less expensive than metastable Eu^{2+}, but Eu^{3+} does not produce a storage phosphor [25, 26].

Weber *et.al.* showed that partial conversion of $EuCl_3$ to $EuCl_2$ can be accomplished by heating it. However, at room temperature in normal atmosphere, it oxidizes to $EuCl_3$ within 10 weeks, so synthesized $EuCl_2$ must be stored in an inert environment [25].

CHAPTER 2

MATERIALS & METHODS

Sample Preparation

All samples were produced in an inert argon atmosphere in an MBraun **LAB**master **SP** glovebox with an attached OTF-1200-2 dual zone tube furnace (MTI Corporation). Oxygen and moisture contamination inside the glove box was monitored. H_2O and O_2 levels below 20 ppm are acceptable, and we generally maintained these levels at <0.1 ppm. A thermocouple is installed inside the ceramic tube in the furnace, near the location of the sample to accurately know the temperature surrounding the sample during the melting process. The furnace was continually purged with argon gas during the melting process. All chemical components were anhydrous which were opened and stored in the glovebox. The system setup is shown in Figure 2.

Figure 2. Glovebox with attached tube furnace used to prepare samples

Glass Synthesis

A series of six fluorochlorozirconate (FCZ) glass samples was produced with the 2% $EuCl_2$ substituted in 0.4% increments by HoF_3. An additional FCZ sample, void of any rare earth dopant, was made for comparison. Table 1 shows the composition of each $EuCl_2$/HoF_3 sample. All chemical constituents were purchased from Sigma Aldrich (Milwaukee, WI).

Table 1. Composition (mole %) of each glass sample produced with HoF_3 replacing $EuCl_2$ in 4% increments and a sample without rare earth dopant

$EuCl_2$/HoF_3 Series Composition (mole %) (20 g Samples)								
Sample	ZrF_4	$BaCl_2$	NaF	AlF_3	LaF_3	InF_3	$EuCl_2$	HoF_3
JJ147	53.00	20.00	20.00	3.00	3.50	0.50	0.00	0.00
JJ138	51.00	20.00	20.00	3.00	3.50	0.50	2.00	0.00
JJ146	51.00	20.00	20.00	3.00	3.50	0.50	1.60	0.40
JJ145	51.00	20.00	20.00	3.00	3.50	0.50	1.20	0.80
JJ144	51.00	20.00	20.00	3.00	3.50	0.50	0.80	1.20
JJ143	51.00	20.00	20.00	3.00	3.50	0.50	0.40	1.60
JJ142	51.00	20.00	20.00	3.00	3.50	0.50	0.00	2.00
							Dopant	

Each of the 20 gram glass samples was produced using a two-step process to decrease the evaporation of chlorides during the melt. During the first step, the fluoride compounds (except HoF_3) were weighed, blended in a platinum crucible, covered, and placed in the tube furnace at room temperature. A schematic of the heating process is shown in Figure 3 and corresponds to the temperature recorded by the thermocouple embedded within the furnace. Each sample underwent a two hour drying stage as the furnace ramped to 800° C. After one hour at 800° C, the melted fluoride mixture was removed and cooled to room temperature. During the second step, the chloride compounds and HoF_3 were added to the solidified fluorides and the mixture was returned to the 750° C furnace. The glass mixture spent one hour at 750° C, five minutes as the furnace ramped to 700° C, and an additional five minutes at 700° C. Decreasing the temperature during the final ten minutes of the melting process fines the glass and reduces the bubbles in the poured sample. The temperature program is shown Appendix I.

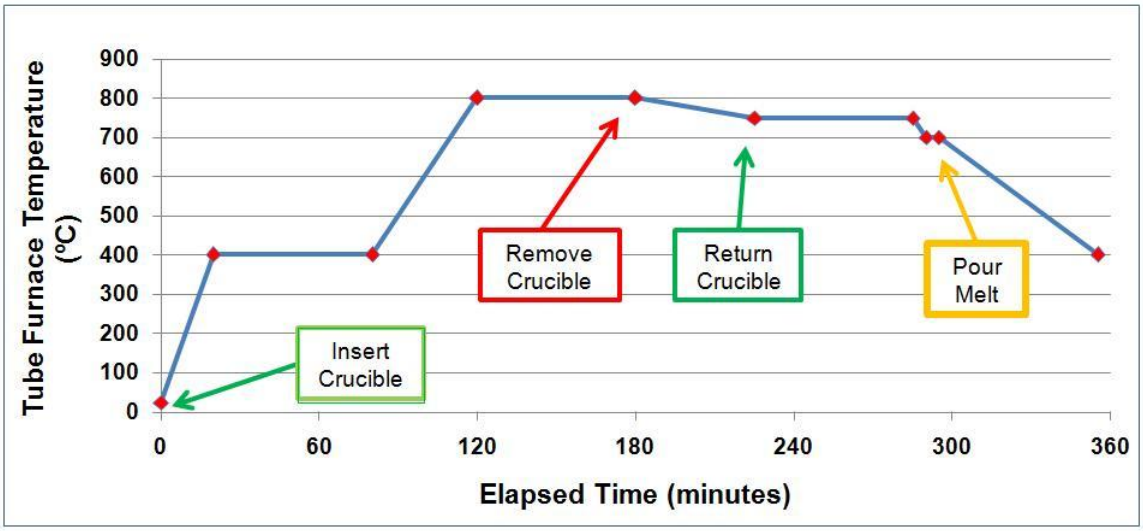

Figure 3. Schematic of Temperature Profile used for glass synthesis

Each sample was removed from the furnace and poured into a preheated 200° C brass mold that was pre-programmed to slowly return to room temperature over four hours. The procedure is shown in Figure 4. The mold has two embedded cartridge heaters which heat the mold and an embedded thermocouple which monitors the temperature. The rapid temperature change from 700° C, when the sample is removed from the furnace, to 200° C, which is just below the glass transition temperature, ensures that the sample transitions rapidly through crystallization formation temperatures, effectively suppressing any crystallization reactions.

After reaching room temperature, the amorphous glass samples were removed from the mold. A typical sample is shown in Figure 5. The glass samples were cut into 1 cm^2 sections for heat treatments and characterization. They were stored inside the glove box in an inert environment to prevent contamination due to the atmosphere.

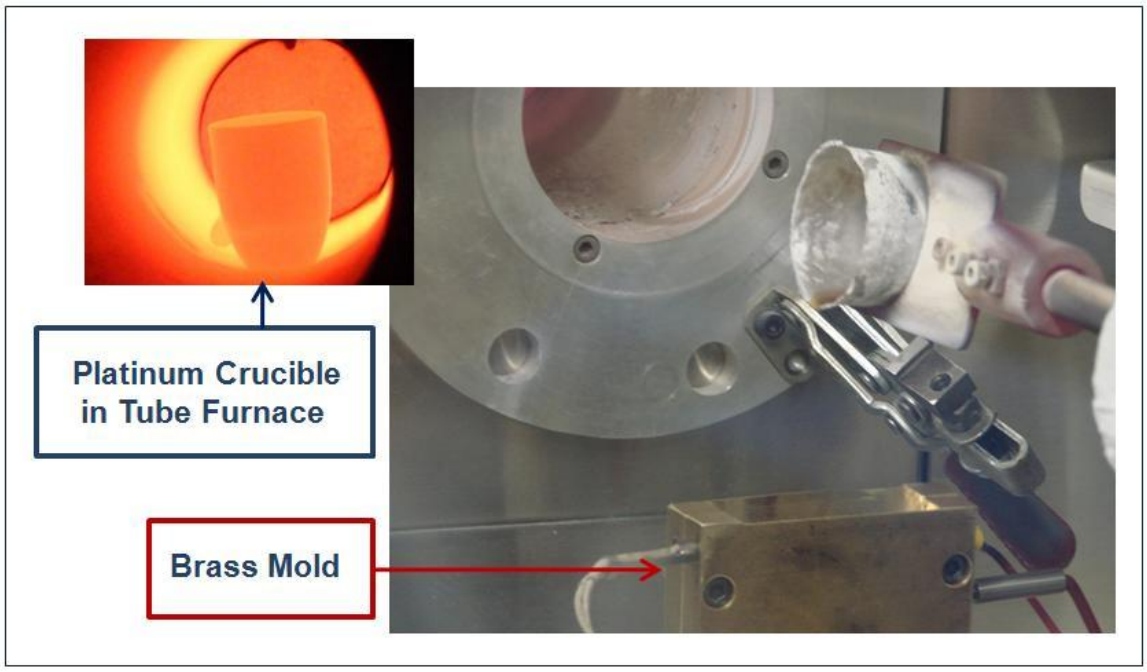

Figure 4. Platinum crucible inside the furnace and during the pour process

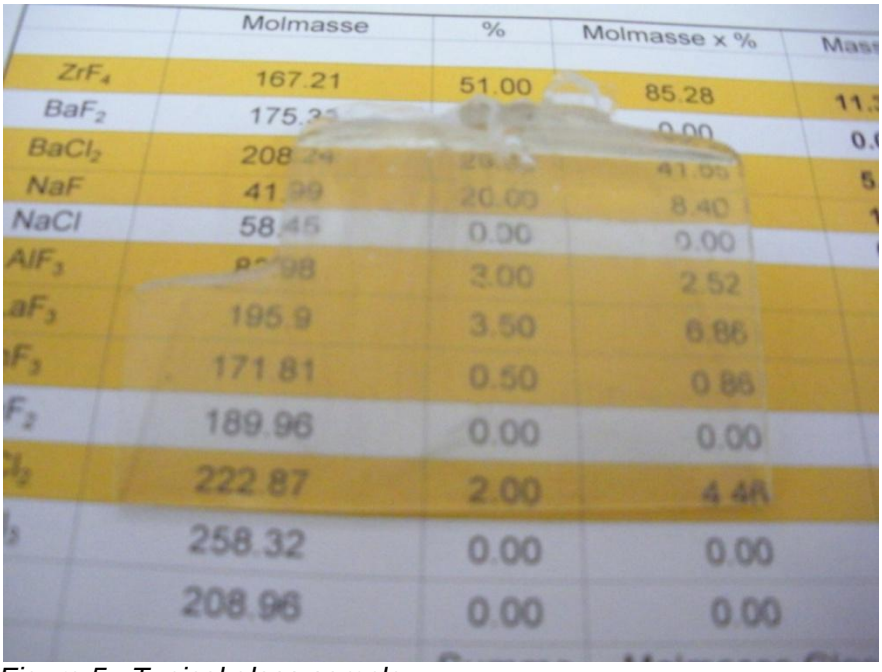

Figure 5. Typical glass sample

Glass Ceramic Synthesis

Thermal treatment determines the specific $BaCl_2$ crystalline phase present in FCZ glass. At lower temperatures (near 235° C), hexagonal phase $BaCl_2$ crystallites form. These make good scintillators. At higher temperatures (near 290° C), orthorhombic phase $BaCl_2$ crystallites precipitate. The orthorhombic nanocrystals produce the crystal defects required to produce effective storage phosphors [18, 36]. During the heat treatment, the rare earth ions ($EuCl_2$) associate with the $BaCl_2$ and become incorporated into the crystallite structure. The crystallites are randomly oriented in the glass [20].

The 1 cm^2 sample pieces were heat treated at temperatures corresponding to hexagonal and orthorhombic phase $BaCl_2$ crystallization as well as the temperature when bulk crystallization occurs. Glass ceramic samples heat treated to precipitate hexagonal phase $BaCl_2$ nanocrystals are not within the scope of this investigation since they have potential photovoltaic applications and do not have storage phosphor applications. The samples with hexagonal $BaCl_2$ nanocrystals and those heat treated at the bulk crystallization temperature are included for comparison purposes only. Table 2 lists thermal treatments performed to precipitate orthorhombic phase $BaCl_2$ nanocrystals required for storage phosphors. Heat treatment temperatures were determined by differential scanning calorimetry analysis.

Table 2. Heat treatments performed to precipitate orthorhombic nanocrystals

Composition $EuCl_2/HoF_3$	Pre-heat (ºC)	Heat Treatment (ºC) (Orthorhombic Phase)
0.0/0.0	207	299
2.0/0.0	208	297
1.6/0.4	209	299
1.2/0.8	205	300
0.8/1.2	209	298
0.4/1.6	210	294
0.0/2.0	209	298

To prevent thermal shock during heat treatment, samples were preheated for five minutes at 205º - 210º C to just below the glass transition temperature. The system setup is shown in Figures 6 and 7. A hot plate was used to heat an

aluminum block with an embedded thermocouple to the preheat temperature. Samples were placed on a tray on the heated surface.

Either a Carbolite three zone tube furnace or an Electro Applications Inc. tube furnace was used to heat treat samples. Each sample was placed in a preheated covered aluminum boat with embedded thermocouple and returned to the oven for five minutes at the desired temperature. Temperatures were monitored and recorded every minute during the process. Samples were removed from the furnace to the 200° C heated tray and allowed to return to room temperature.

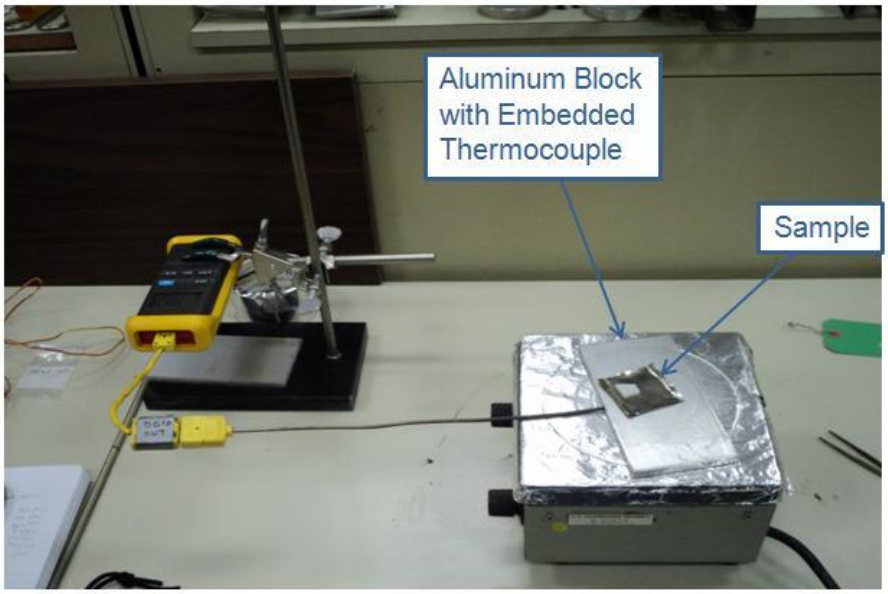

Figure 6. Samples were pre-heated to just below the glass transition temperature to prevent thermal shock

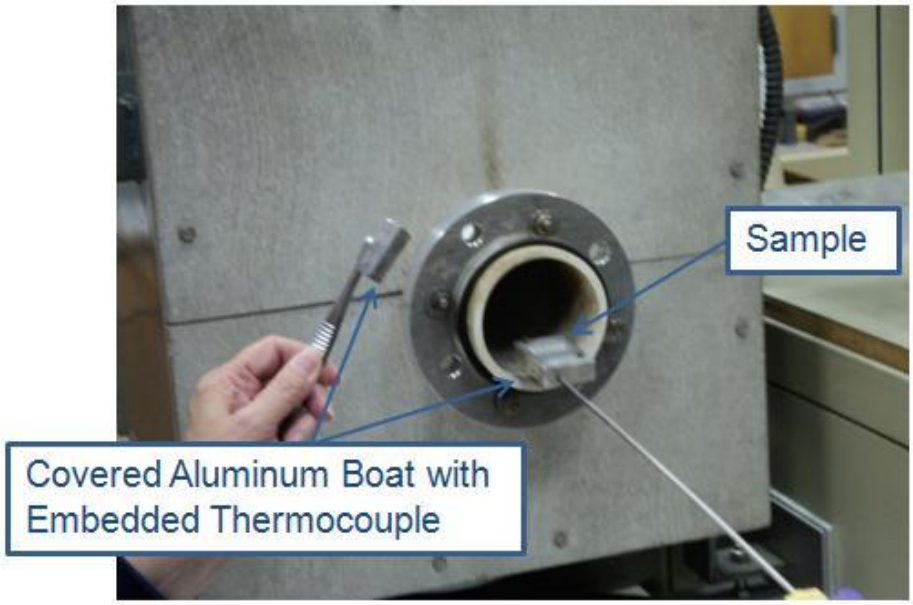

Figure 7. Thermal treatment furnace setup

After heat treatment, samples exhibit unique color changes when exposed to ultraviolet light. Color is the first visual indicator of the specific $BaCl_2$ phase present in the samples. Blue fluorescence suggests presence of hexagonal phase and purple suggests presence of orthorhombic phase nanocrystals.

This is illustrated in Figure 8 (left) when samples were exposed to 254 nm excitation wavelength and (right) to 365 nm excitation wavelength. Column one contains doped samples that have not undergone any heat treatment. Column two contains samples heat treated at 250º C to precipitate hexagonal phase $BaCl_2$ crystallites. Column three holds samples heat treated at 300º C to precipitate orthorhombic phase $BaCl_2$ crystallites. Column four contains samples that were heat treated to 330º C, the bulk crystallization temperature.

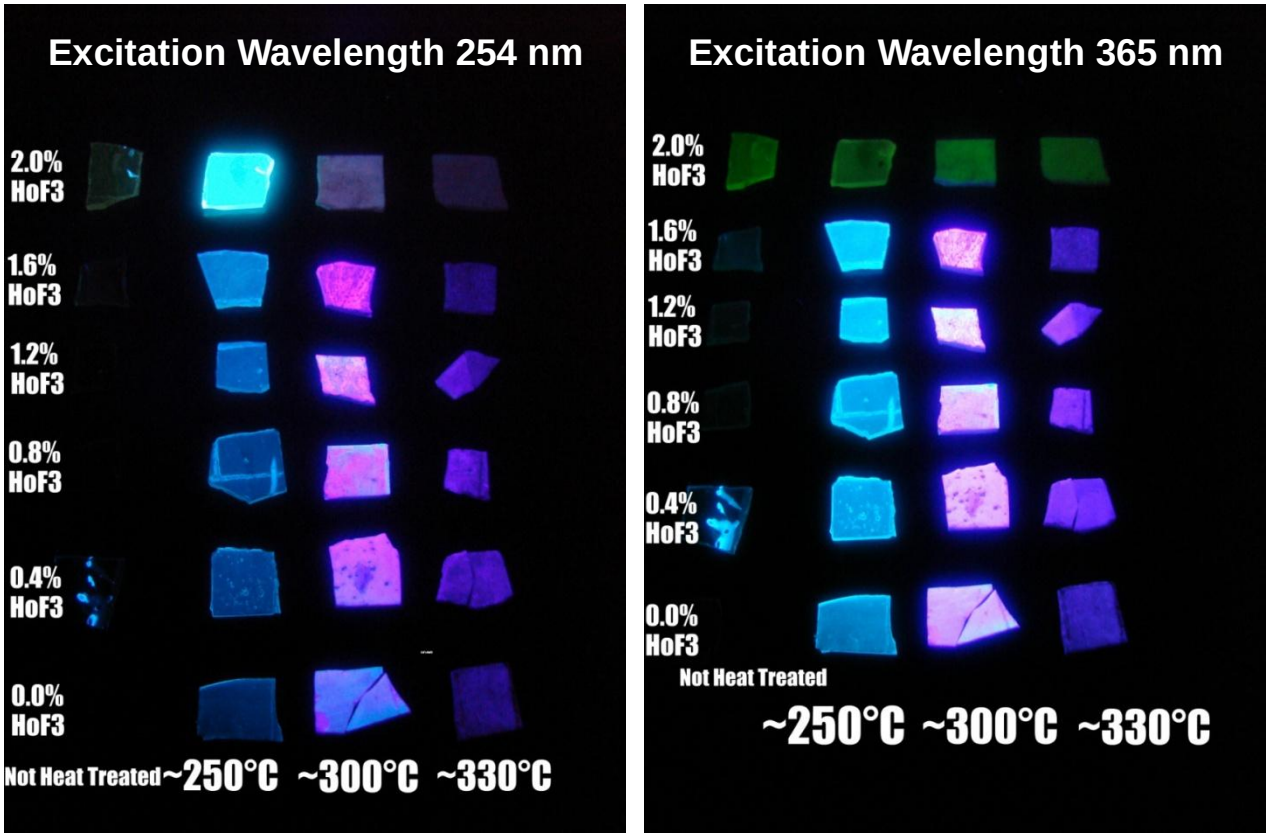

Figure 8. Unpolished, doped samples exposed to 254 nm and 365 nm ultraviolet excitation

$EuCl_3$ Reduction/$EuCl_2$ Synthesis

Rare earth dopants are critical for producing an effective storage phosphor. Cuts in production have led to limited availability and higher costs. The Eu^{3+} state is stable and less expensive than the Eu^{2+} state. $EuCl_3$ doped FCZ does not generate crystal defects required to produce a storage phosphor material.

Experiments to determine an optimal temperature program for reducing $EuCl_3$ to $EuCl_2$ were carried out in the glovebox and tube furnace shown in Figure 2. Anhydrous $EuCl_3$ was purchased from Sigma-Aldrich (Milwaukee, WI). It was weighed, placed into a platinum crucible, covered, inserted into the tube furnace, and heated at 700° C. Three samples were produced using different heating profiles. The temperature and time profiles are shown in Figures 9, 10, and 11.

During the first two hours, the oven is ramped in increments to prevent thermal shock to the ceramic tube in the furnace. One sample was placed in the furnace to undergo the ramping stage and then heated at 700° C for one hour. The other two samples were inserted into the 700° C furnace at the end of the ramping stage. One was heated for one hour and the other was heated for six hours. The oven temperature programs are shown in Appendix II.

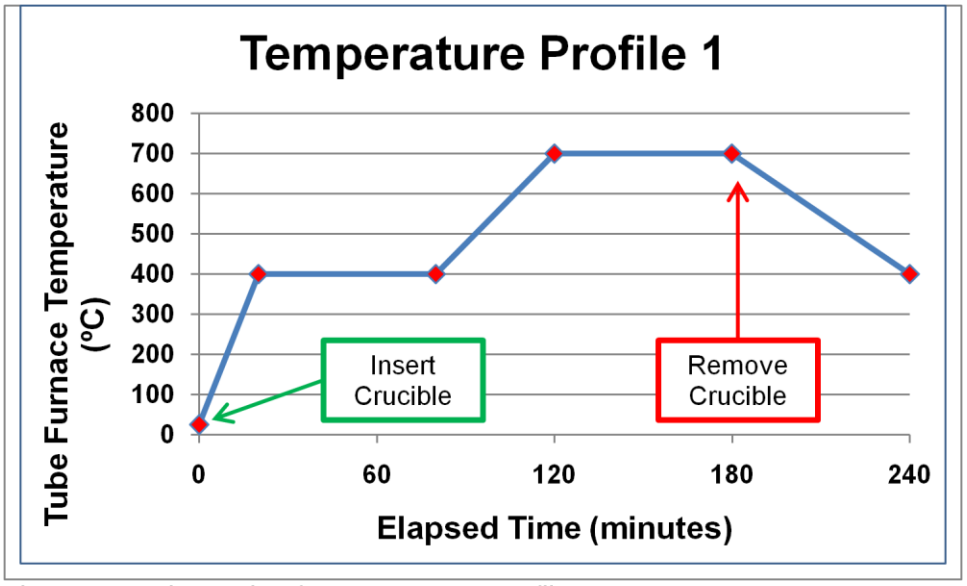

Figure 9. Schematic of Temperature Profile 1

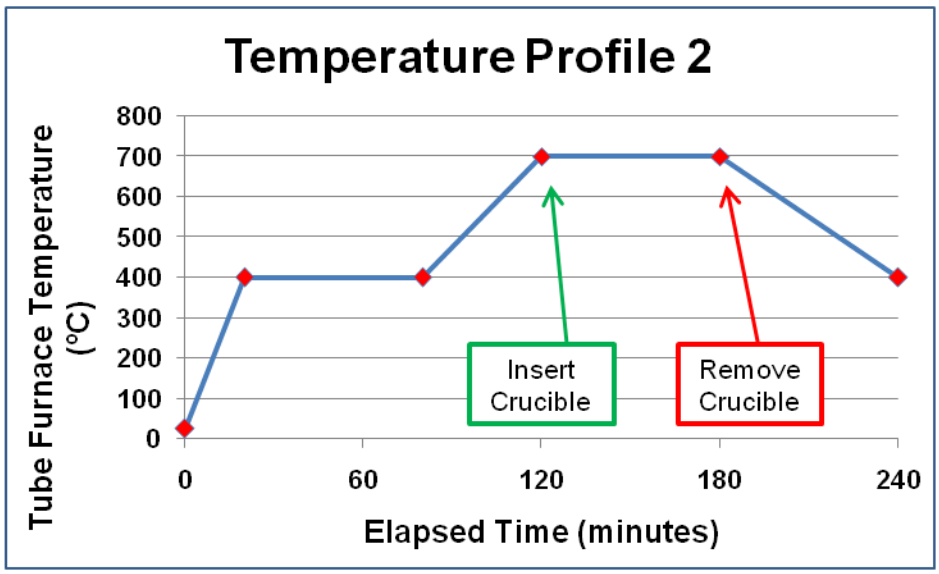

Figure 10. Schematic of Temperature Profile 2

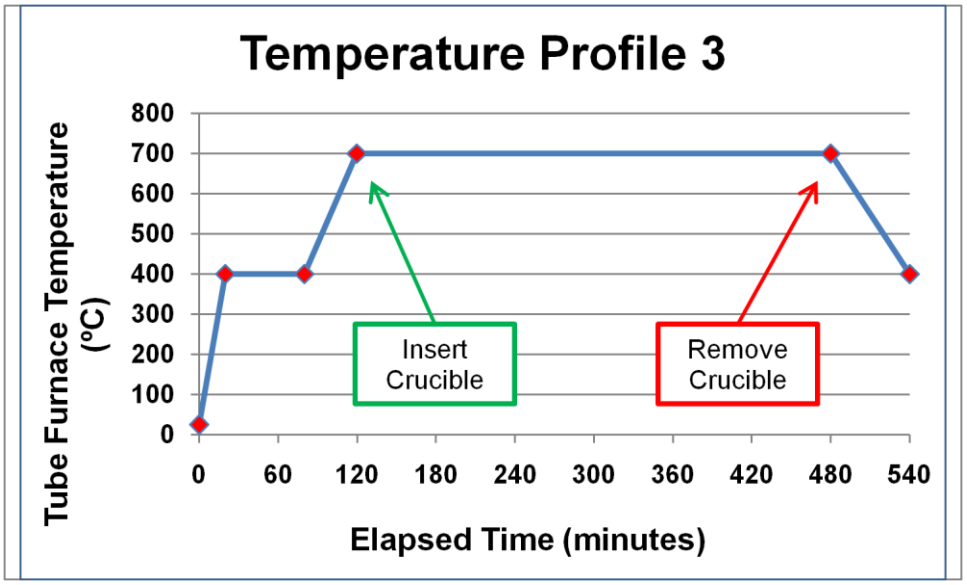

Figure 11. Schematic of Temperature Profile 3

The samples were removed from the furnace, cooled to room temperature, and finely powdered with a mortar and pestle. A thin layer of vacuum grease was applied to a sample holder and the powder was attached. Samples were stored in the glovebox at room temperature or in a VWR Signature ULT Freezer Model 5600 Series Chest freezer at -80° C (193 K).

Characterization

Amorphous “as made” glass samples were characterized using differential scanning calorimetry to determine the temperatures specific to each crystallization phase. After heat treatments were performed to precipitate orthorhombic nanocrystals, the glass ceramic samples were characterized using phosphorimetry and x-ray diffraction. Photostimulated luminescence analysis was used to determine the conversion efficiency or light output of the samples. Mössbauer spectroscopy was used to measure $EuCl_2$ and $EuCl_3$ concentrations in samples produced by heating $EuCl_3$.

Differential Scanning Calorimetry (DSC)

Differential Scanning Calorimety (DSC) was used to determine the glass transition temperature (T_g) and the temperatures where crystallization occurs. Measurements were acquired using a Netzsch DSC 200 F3 (NETZSCH, Geraetebau GmbH, Willelsbacherstrasse 42 D-95100 Selb/Bayern), and analysis was performed using Netzsch Proteus Thermal Analysis Version 5.2.1.

Small fragments (20 mg ±10 mg) were selected from the interior bulk of each sample. For each measurement, the fragment was placed in a standard Netzch Aluminum 25 µl crucible and sealed with a companion lid. The sample was aligned on a heat sensor in the DSC chamber (see Figure 12). An empty sealed crucible was used as a reference and placed on the second heat sensor. During the process, the chamber was continually purged with nitrogen (40 ml/min.) Each DSC measurement was started when the chamber temperature reached 100° C. The temperature increased 10° C per minute to the maximum temperature of 400° C.

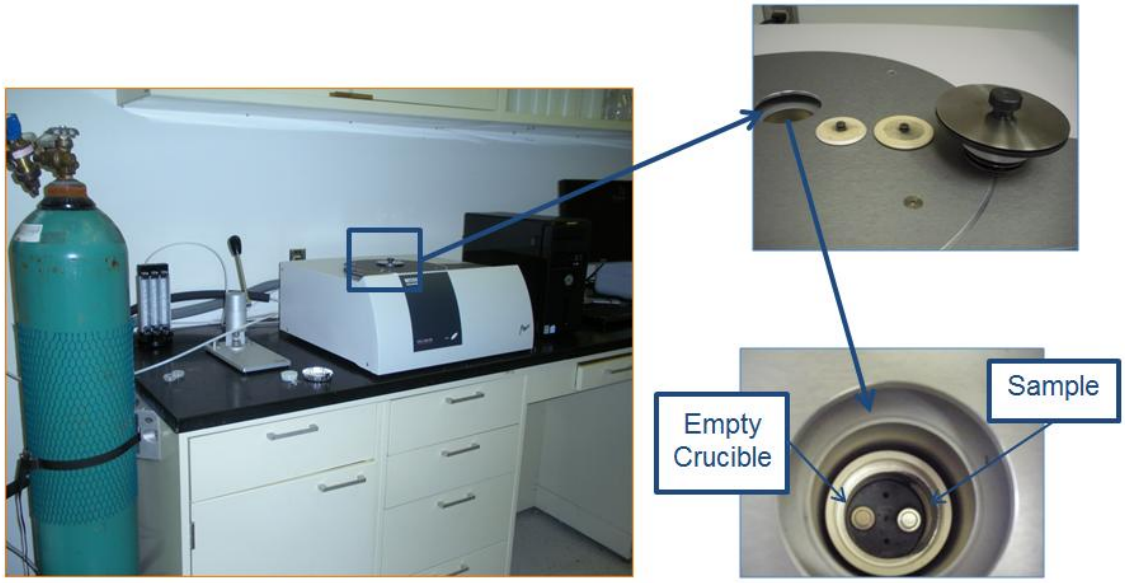

Figure 12. Netzsch200 F3 Differential Scanning Calorimeter used for DSC Analysis

Phosphorimetry (PL)

Phosphorimetry (PL) was used to determine the states of crystallization phases present within each sample. Gated excitation scans excite a sample within a particular range of wavelengths to determine the amount of emission at a specific wavelength. Gated emission scans excite at a specific wavelength to determine emission over a range of wavelengths. The emission scans show the relative amounts of each crystallization phase present. Gated excitation and emission spectra were acquired using a PTI QuantaMaster 30 Phosphorescence / Fluorescence Spectrofluorometer (Birmingham, NJ) in conjunction with PTI Felix32 analysis software. The system configuration is shown in Figure 13.

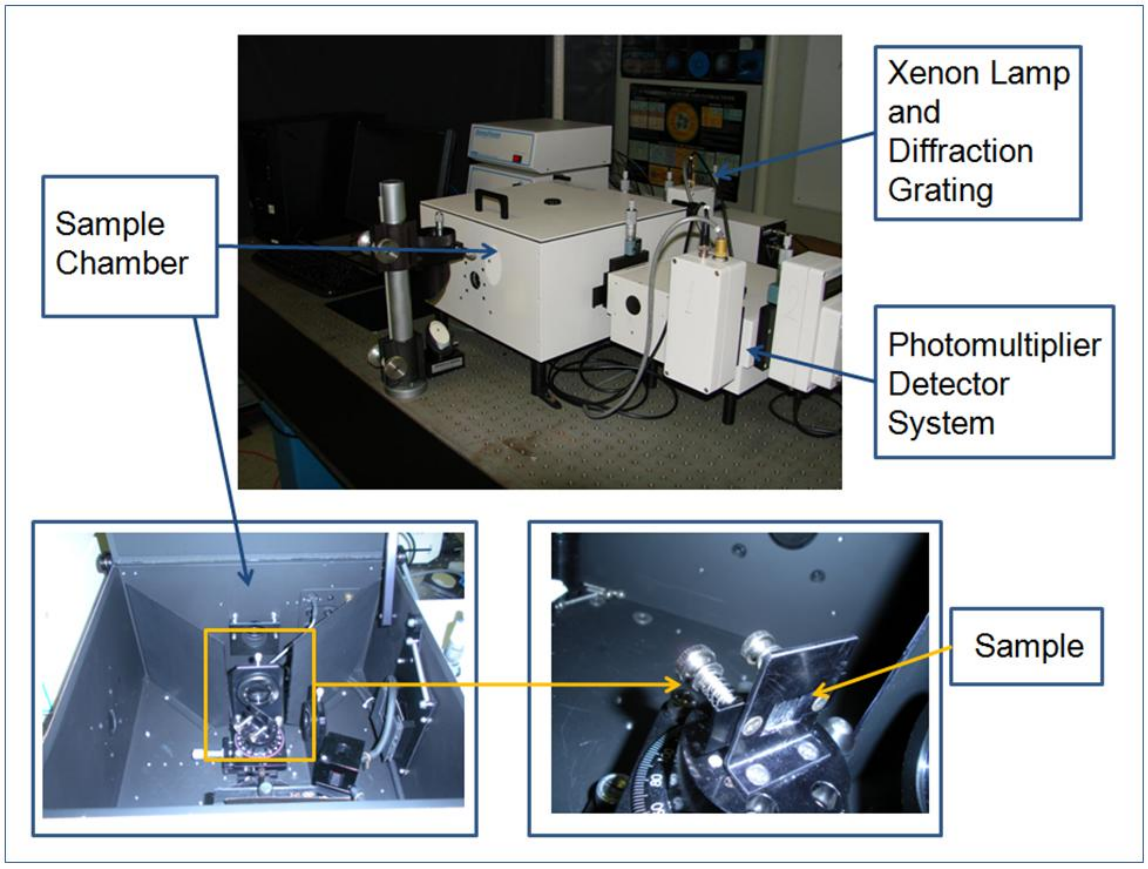

Figure 13. Configuration of PTI QuantaMaster 30 Phosphorescence / Fluorescence Spectrofluorometer used to acquire PL measurements

Samples were polished to expose the bulk and remove surface contamination. Measurements are acquired in a darkened room to eliminate potential light contamination. Table 3 lists the excitation and emission scans acquired for each glass ceramic sample.

Table 3. Gated Excitation and Emission Scans performed on each glass ceramic sample

Gated Excitation Scans		Gated Emission Scans	
Wavelength Range (nm)	Emission Wavelength (nm)	Excitation Wavelength (nm)	Wavelength Range (nm)
225-400	410	270	280-700
225-460	470	360	370-700
225-535	548	448	460-700

X-Ray Diffraction (XRD)

X-Ray diffraction (XRD) was used to identify specific crystallization phases present in the glass ceramic samples. All samples were polished to expose the bulk of the glass prior to measurements.

XRD characterization was performed using a Scintag, Inc. X_1 Advanced Diffraction System XRD and a Philips X'Pert XRD to acquire diffraction patterns. Both systems use Cu Kα radiation (λ = 1.54 Å). The Scintag system is shown in Figures 14a and 14b. All characteristic x-rays are produced. A monochromatic filter permits the detector to count only reflected Cu Kα x-rays. Measurements were taken by continuously scanning the two theta range from 20° to 80° at a rate of 5 degrees per minute.

Figure 14(a). X_1 Advanced Diffraction System, Scintag Inc. Vanderbilt University Chemistry Department

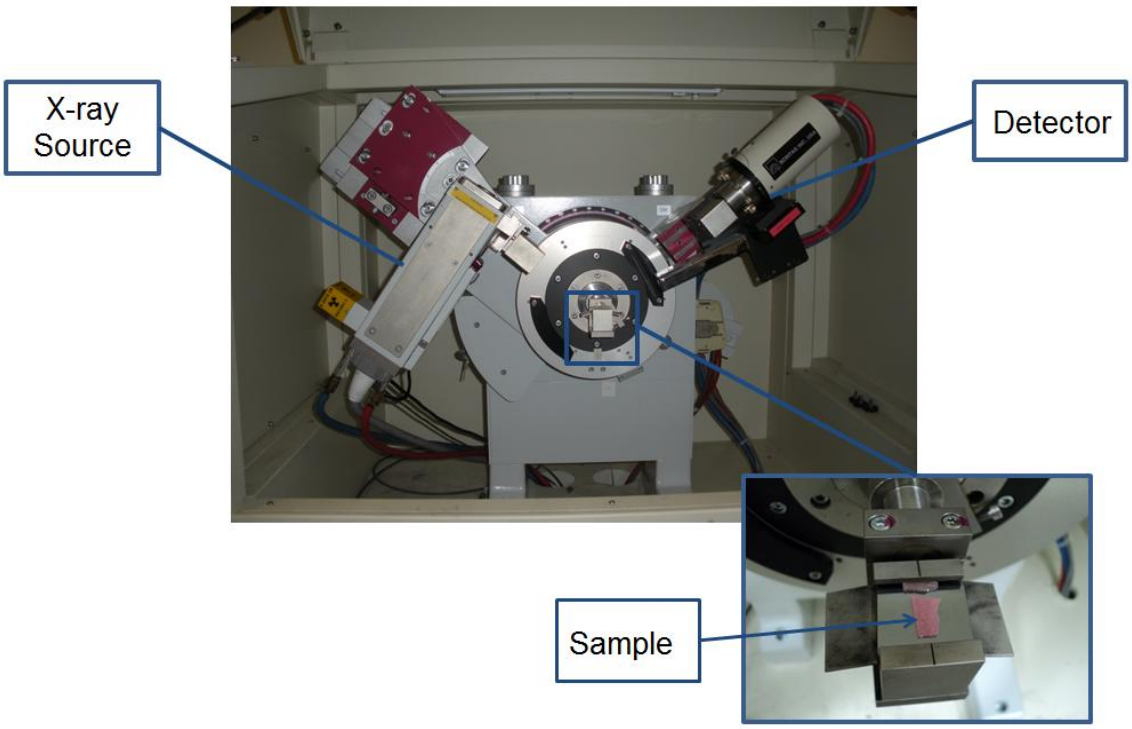

Figure 14(b). The sample is stationary in the horizontal position. The X-ray tube and detector move simultaneously over the angular range

Other experiments were performed using a Philips X'Pert XRD shown in Figure 15. The ceramic tube with copper anode is equipped with a crystal monochrometer so only Cu Kα radiation strikes the sample. Measurements were taken over the two theta range from 20° to 80°using a scanning step of 0.01° and a time step of 4 seconds.

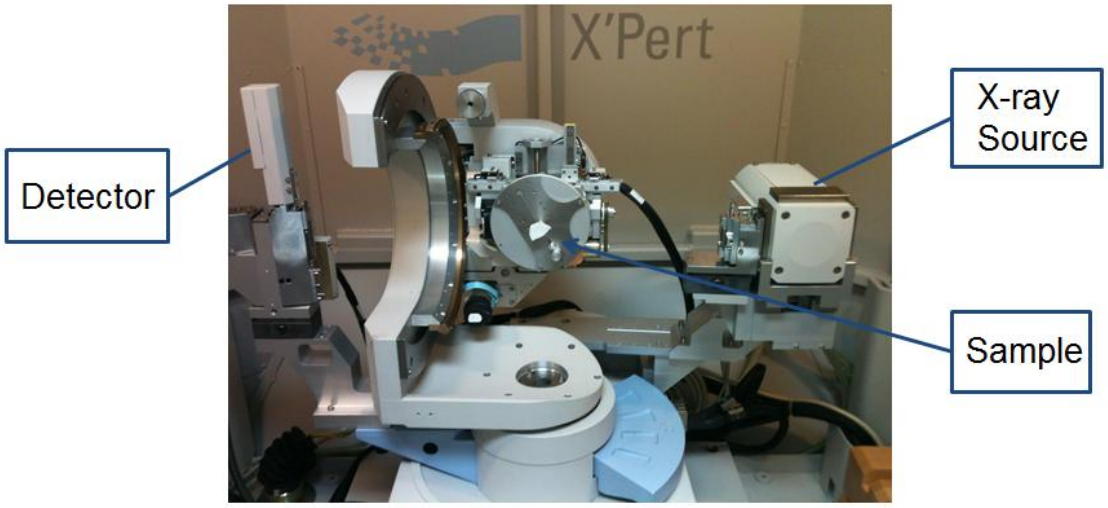

Figure 15. For this goniometer configuration (Philips X'Pert XRD), the x-ray tube is stationary. The sample is positioned vertically and moves with the detector over the angular range

MDI Jade 9 analytical software was used to identify the crystalline phases. The characteristic diffraction pattern obtained for each sample was matched to the Jade database containing diffraction pattern files.

Photostimulated Luminescence (PSL) Analysis

Photostimulated luminescence (PSL) was used to measure the storage phosphor conversion efficiency (CE). CE is the intrinsic efficiency of a storage phosphor to convert x-ray energy into visible light.

$$\text{Conversion Efficiency} = \frac{\text{Output Energy}}{\text{Input Energy (absorbed x-ray dose)}}$$

PSL decays under continuing stimulation according to $I(t) = I_0^{(-t/\tau)}+c$ where I_0 is the amplitude of PSL at beginning of stimulation, t is the stimulation time, τ is a time constant that depends on the power of the stimulation light (exposure speed), and c is a constant which is the measured offset with no sample in place [22]. A schematic showing the PSL decay is shown in Figure 16.

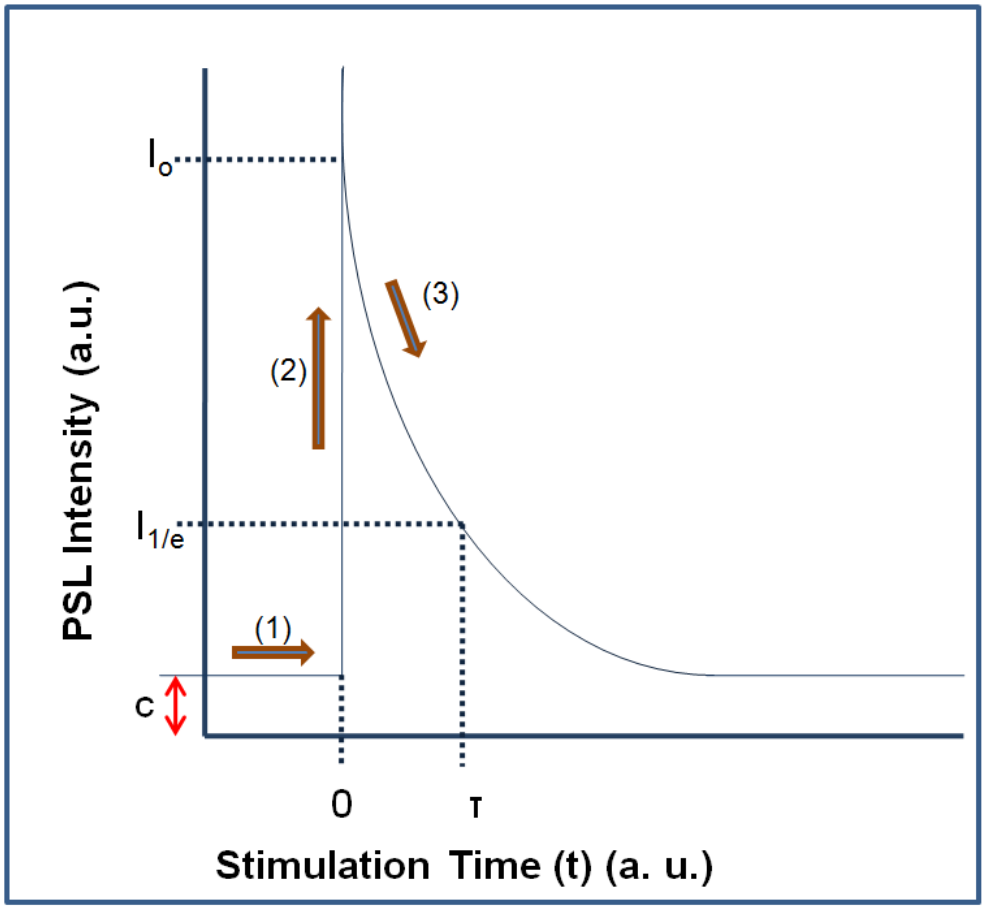

Figure 16. Schematic of PSL curve showing (1) stimulating radiation (2) shutter opening (3) decay curve

Information needs to be read out in the shortest time possible. Ideally there should be a high initial intensity followed by a rapid decay. Otherwise, when a storage phosphor plate is being raster scanned, excess emission of light from the previous pixel may bleed over and corrupt the image.

Dr. Lubinsky performed these experiments at the State University of New York (SUNY), Stony Brook. Figure 17 shows the experimental setup. Initially, samples were exposed to a 320 mRad dose using a Tungsten anode x-ray tube. The apparatus used to test the conversion efficiency is based on an integrating sphere. The stimulating light power of 8.2 mW at 532 nm was spread by a diffuser over an area about 8x10 mm. The sample port has a 1/8 inch opening. A red-cutting filter and two 2mm FBG25 Thorlabs filters were used to prevent detection of the stimulating light. The detector is a Hamamatsu 124-06 module with an R6095 photomultiplier tube which was operated at 700V.

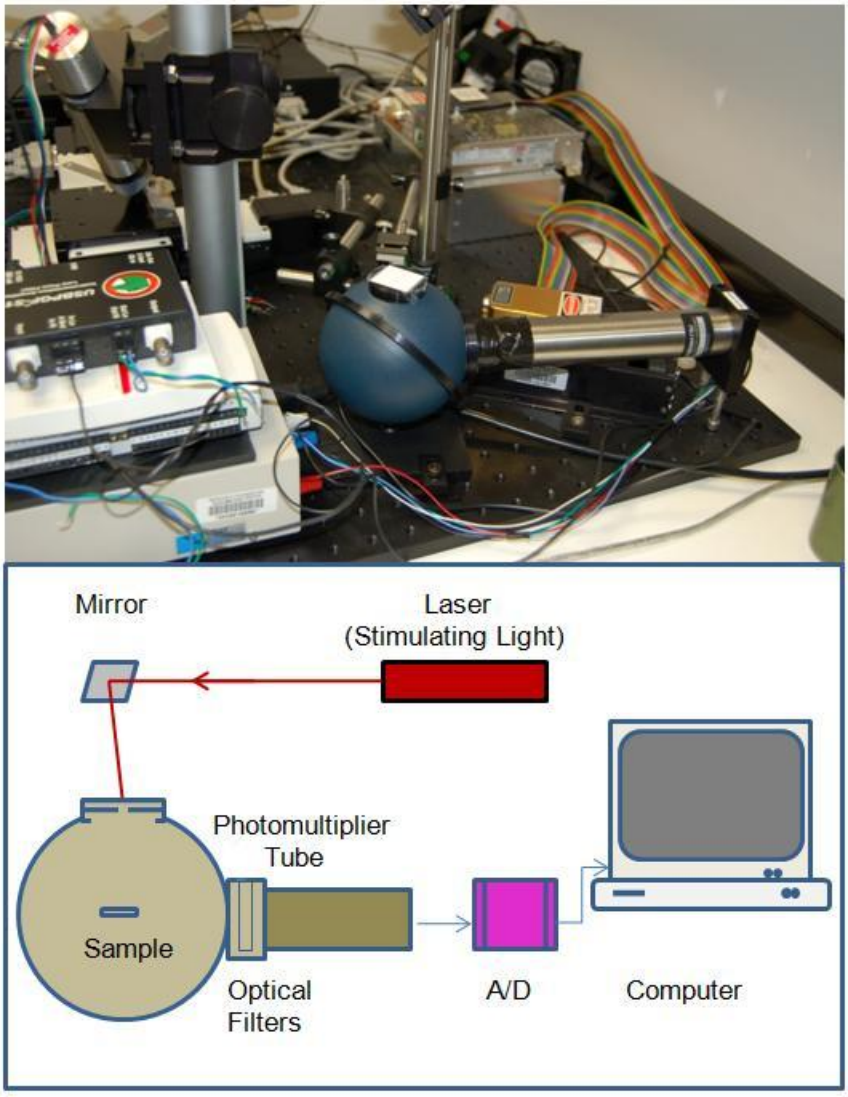

Figure 17. Apparatus based on integrating sphere used to determine conversion efficiency

Mössbauer Spectroscopy

Mössbauer spectroscopy was used to measure the relative concentrations of $EuCl_2$ and $EuCl_3$. The measurements were acquired using a SEE Co Mössbauer Spectrometer (Minneapolis, MN) with Janis model SHI-850-5 closed cycle refrigerator system with operation capacity of 5K-300K (Willmington, MA). The cryogen-free, continuous flow cryostat was used to measure relative concentrations at low temperatures. The apparatus is shown in Figures 18 and 19.

Spectroscopy measurements were obtained for samples at temperatures between 5K and 250K. At room temperature, the Mössbauer Effect is reduced due to thermal vibration. By measuring the sample in a cryostat at lower temperatures, there is less thermal vibration, and the Mössbauer Effect is much more detectable.

A Mössbauer data analysis program created at Northern Illinois University was used to fit the spectra. This software was designed to fit Mössbauer spectra using simple Lorentzian functions.

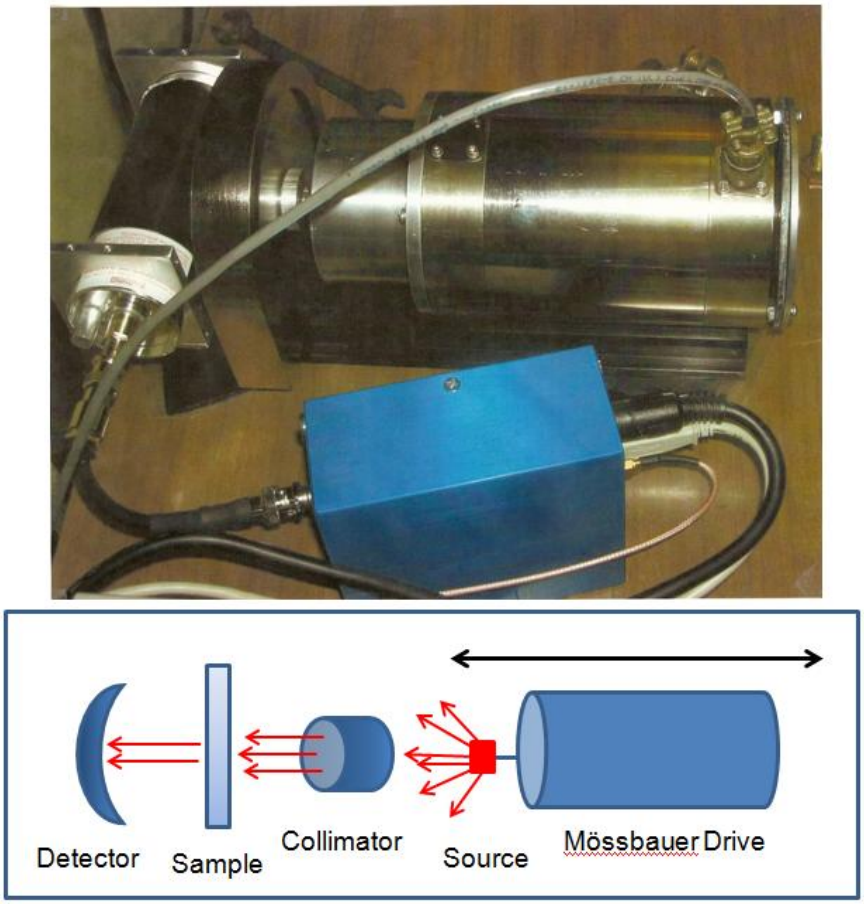

Figure 18. Mössbauer spectrometer showing Detector (proportional counter), Sample, Collimator, Source at room temperature (^{151}Sm in Eu_2F_3), and the Mössbauer Drive (velocity transducer)

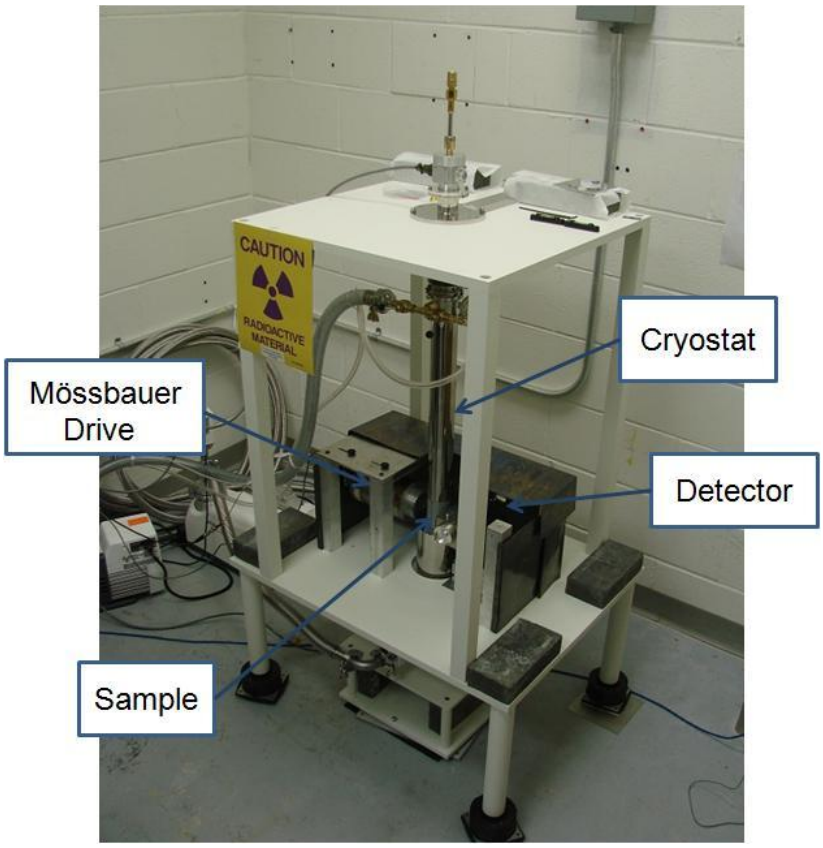

Figure 19. Mössbauer apparatus with cryostat used for low temperature experiments

CHAPTER 3

RESULTS & DISCUSSION

$EuCl_2/HoF_3$ Co-doped FCZ Glass Ceramics

Differential Scanning Calorimetry (DSC)

DSC scans on each of the "as made" glass samples are stacked for comparison in Figure 20. The spectra follow the profile consistent with $BaCl_2$ crystallite formation in either hexagonal or orthorhombic phase. The first exothermal peak occurs at 240 °C (± 3° C) and indicates the formation of the hexagonal phase of $BaCl_2$. The second exothermal peak occurs at 300 °C (± 5° C) and shows the formation of the orthorhombic phase of $BaCl_2$.

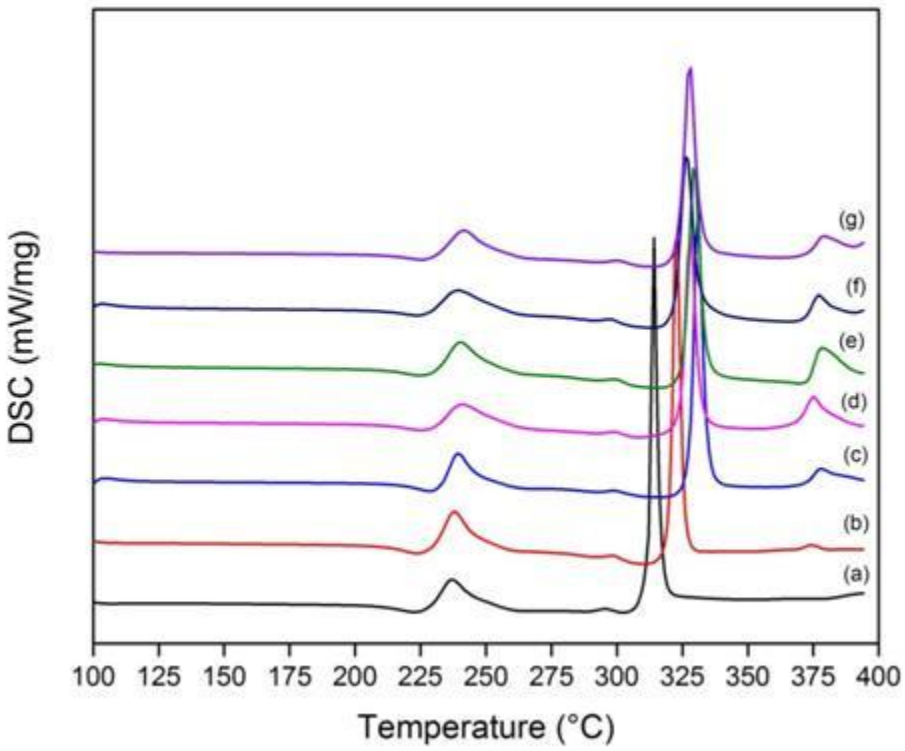

Figure 20. DSC scan comparison for (a) undoped ZBLAN and (b-g) in which the $EuCl_2$ dopant was exchanged with HoF_3 dopant in 0.4% increments as follows: (b) / 2.0% $EuCl_2$ / 0.0% HoF_3 (c) 1.6% $EuCl_2$ / 0.4% HoF_3 (d) 1.2% $EuCl_2$ / 0.8% HoF_3 (e)0.8% $EuCl_2$ / 1.2% HoF_3 (f)0.4% $EuCl_2$ / 1.6% HoF_3 (g)0.0% $EuCl_2$ / 2.0% HoF_3

The third exothermal peak is attributed to bulk crystallization of the glass matrix [16, 28]. The sample without dopant undergoes bulk crystallization at a lower temperature (314° C) than the $EuCl_2$ doped sample (322.7° C). The HoF_3 doped samples underwent bulk crystallization at higher temperatures (329° C ± 3° C). Exothermal peaks at higher temperatures are due to reactions between crystalline phases and crystal consolidation [13]. Analysis data is shown in Table 4.

Table 4. Temperatures at which hexagonal and orthorhombic $BaCl_2$ form and the temperatures when bulk crystallization of the glass matrix occurs

% $EuCl_2$	% HoF_3	Glass Transition (°C)	Peak 1 (°C) $BaCl_2$ (hexagonal)	Peak 2 (°C) $BaCl_2$ (orthorhombic)	Peak 3 (°C) Bulk Crystallization
0.0	0.0	208.4	237.0	295.4	314.0
2.0	0.0	212.3	238.0	297.9	322.7
1.6	0.4	217.5	239.3	298.7	330.9
1.2	0.8	212.2	241.1	298.5	328.0
0.8	1.2	212.2	240.2	298.9	329.5
0.4	1.6	212.6	239.4	297.1	326.5
0.0	2.0	211.1	241.5	299.7	327.7

The glass transition (T_g) occurs near 213 °C (± 5° C) for all the samples. The temperature difference between the glass transition (T_g) and crystallization (T_x) is an indicator of viscosity ($\Delta T = Tx - Tg$). Larger temperature difference (ΔT) equates to less viscous glass [16]. Inclusion of HoF_3 changes the viscosity of the glass more than the inclusion of $EuCl_2$.

Phosphorimetry (PL)

Gated emission scans show phosphorescence is dopant dependent. Each spectrum was normalized, and they are stacked for comparison.

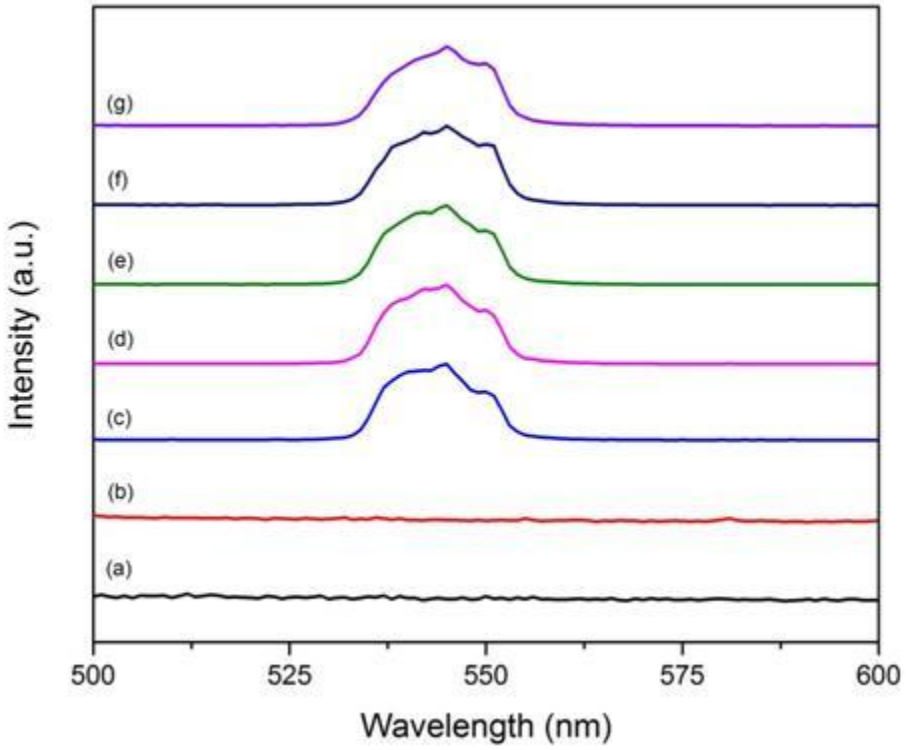

Figure 21. Normalized emission spectra where the samples were excited at 448 nm and observed between 460 and 700 nm for (a) undoped ZBLAN and (b-g) in which the $EuCl_2$ dopant was exchanged with HoF_3 dopant in 0.4% increments as follows: (b) / 2.0% $EuCl_2$ / 0.0% HoF_3 (c) 1.6% $EuCl_2$ / 0.4% HoF_3 (d) 1.2% $EuCl_2$ / 0.8% HoF_3 (e) 0.8% $EuCl_2$ / 1.2% HoF_3 (f) 0.4% $EuCl_2$ / 1.6% HoF_3 (g) 0.0% $EuCl_2$ / 2.0% HoF_3

Figure 21 shows that the phosphorescence resulting from 448 nm excitation is dependent upon the holmium content. The undoped sample and the solely doped $EuCl_2$ sample experience no emission. HoF_3 has a known 550 nm fluorescence which is attributed to the $^5S_2$, $^5F_4 \rightarrow {}^5I_8$ upconversion based upon multiphonon (non-radiative) processes [34, 36].

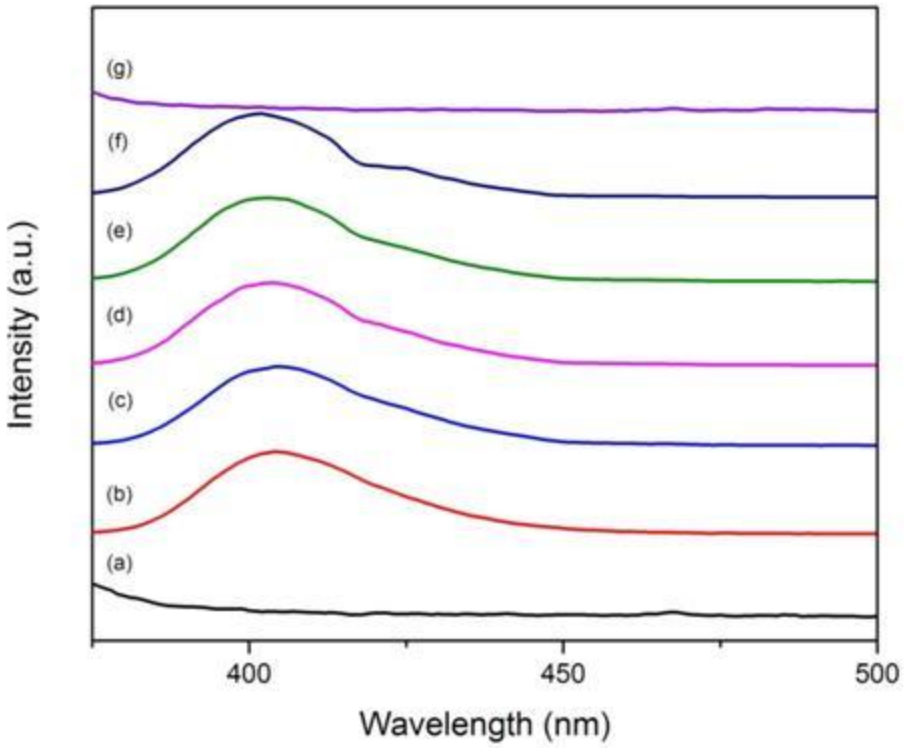

Figure 22. Normalized emission spectra where the samples were excited at 360 nm and observed between 370 and 700 nm for (a) undoped ZBLAN and (b-g) in which the $EuCl_2$ dopant was exchanged with HoF_3 dopant in 0.4% increments as follows: (b) / 2.0% $EuCl_2$ / 0.0% HoF_3 (c) 1.6% $EuCl_2$ / 0.4% HoF_3 (d) 1.2% $EuCl_2$ / 0.8% HoF_3 (e) 0.8% $EuCl_2$ / 1.2% HoF_3 (f) 0.4% $EuCl_2$ / 1.6% HoF_3 (g) 0.0% $EuCl_2$ / 2.0% HoF_3

Phosphorescence occurring when the samples are excited at 360 nm is europium dependent. See Figure 22. Only samples containing $EuCl_2$ experience emission. A divot in the spectra occurs near 418 nm. Samples with greater percentages of HoF_3 exhibit more distinct divots. $EuCl_2$ has a known emission at 402 nm which is attributed to the 5d → 4f transition [18, 24]. The divots in the spectra located near 418 nm may be attributable to HoF_3 absorption at that wavelength due to the $^5I_8 \rightarrow {}^5G_5$ transition. This suggests that some of the $EuCl_2$ emission is absorbed by HoF_3.

X-Ray Diffraction (XRD)

The x-ray diffraction scans are stacked for comparison in Figure 23. XRD peaks were used to identify the $BaCl_2$ phases present in the samples. Powder diffraction file (PDF # 24-0094) is superimposed at the bottom and indicates $BaCl_2$ orthorhombic phase nanocrystals in all the samples.

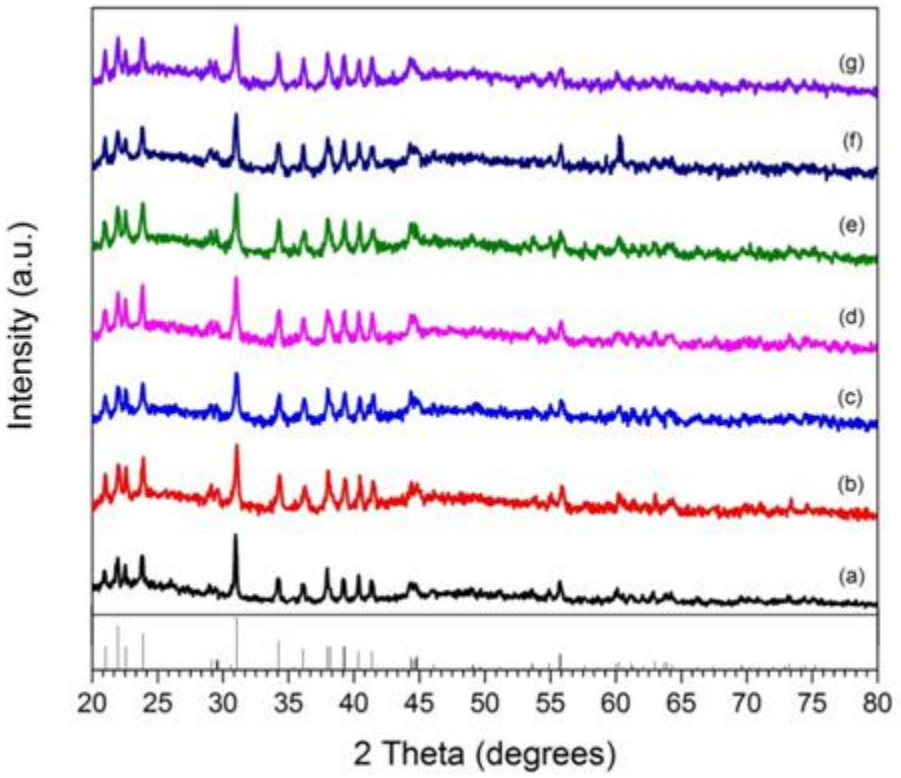

Figure 23. X-ray diffraction scans for (a) undoped ZBLAN and (b-g) in which the $EuCl_2$ dopant was exchanged with HoF_3 dopant in 0.4% increments as follows: (b) / 2.0% $EuCl_2$ / 0.0% HoF_3 (c) 1.6% $EuCl_2$ / 0.4% HoF_3 (d) 1.2% $EuCl_2$ / 0.8% HoF_3 (e) 0.8% $EuCl_2$ / 1.2% HoF_3 (f) 0.4% $EuCl_2$ / 1.6% HoF_3 (g) 0.0% $EuCl_2$ / 2.0% HoF_3

Photostimulated Luminescence (PSL) Analysis

Conversion efficiency results from the PSL experiments are shown in Table 5. The gain, which is the number of photoelectrons per absorbed x-ray, is an absolute number and is an indicator of light output. A comparison of conversion efficiency relative to HoF_3 content is plotted and shown in Figure 24.

Table 5. Conversion efficiency and gain results

$EuCl_2$ %	HoF_3 %	Conversion Efficiency (pJ/mm^2 mRad)	Gain (photoelectrons/ absorbed x-ray)
0.0	0.0	0.0	0.0
2.0	0.0	2.2	1.1
1.6	0.4	2.4	1.2
1.2	0.8	3.4	1.65
0.8	1.2	4.5	2.2
0.4	1.6	4.0	2.0
0.0	2.0	0.0	0.0

The undoped sample and the singly doped HoF_3 sample exhibited no light output while all the co-doped samples have improved light output compared to the singly doped $EuCl_2$ sample. The enhanced conversion efficiency follows a linear trend based upon increased HoF_3 content for samples containing less than 1.6% HoF_3. The highest conversion efficiency was achieved by the sample co-doped with 0.8% $EuCl_2$ and 1.2% HoF_3. Diminished conversion efficiency was experienced by samples containing more than 1.2% HoF_3.

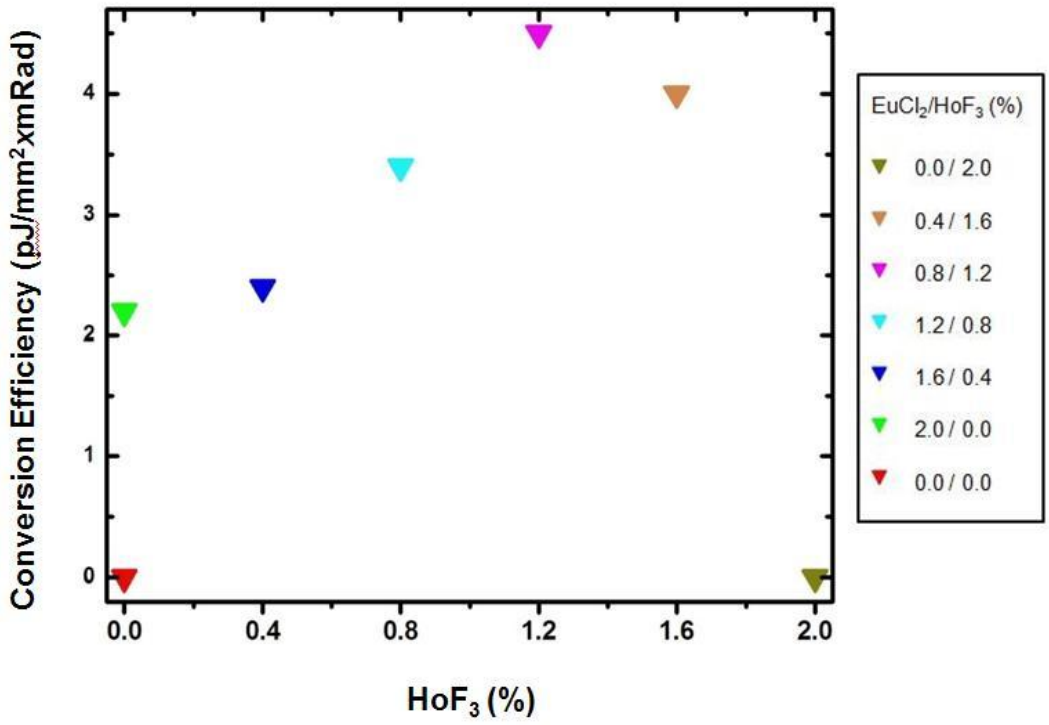

Figure 24. Comparison of conversion efficiency for each sample tested

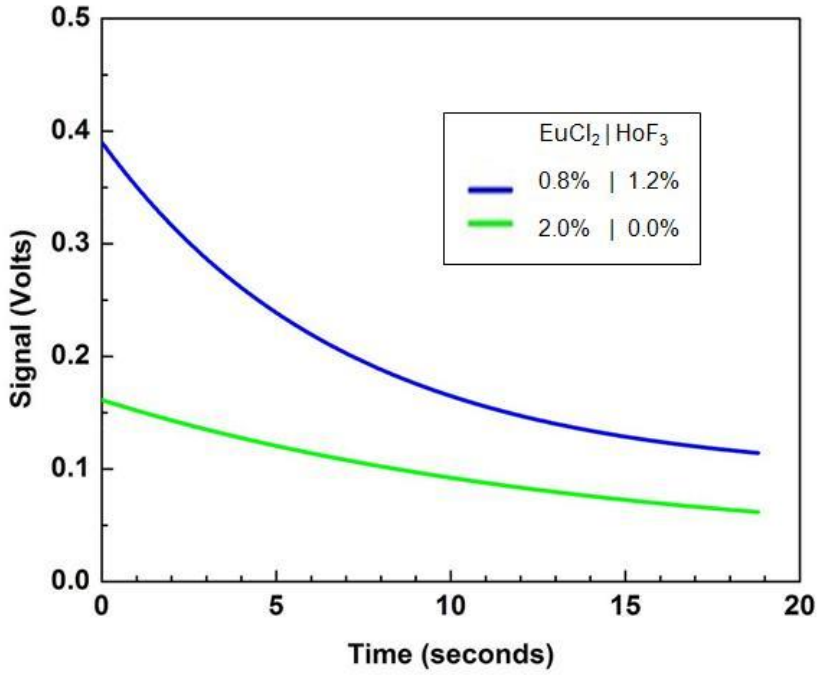

Figure 25. Comparison of light output for samples containing 2% $EuCl_2$/0% HoF_3 and 0.8% $EuCl_2$/1.2% HoF_3

Figure 25 compares the decay curve trend line of the singly doped sample containing 2% $EuCl_2$ and the co-doped sample containing 0.8% $EuCl_2$ and 1.2% HoF_3 which experienced the highest conversion efficiency. An efficient storage phosphor should exhibit the characteristic decay curve shown in Figure 16 with high initial signal and rapid decay. The co-doped sample exhibits significantly superior PSL to the singly doped sample.

These PSL results confirm the necessity of adding rare earth dopants to FCZ glass to produce an efficient storage phosphor. There are several potential causes of the increased PSL in the co-doped samples, including:

1) Increase in $BaCl_2$ nanocrystal precipitation during thermal processing due to HoF_3.

2) More crystal defects formed in $BaCl_2$ nanocrystals which allow more electron hole trapping due to HoF_3.

3) Different nanocrystal size or shape due to HoF_3.

4) Possible energy exchange in luminescence center between HoF_3 and $EuCl_2$.

Additional studies are required to better understand the mechanism that leads to the enhanced PSL. The nanocrystal size and shape analysis can be performed with transmission electron microscopy.

Further testing is necessary to determine if the PSL increase in co-doped samples is due to HoF_3 or $EuCl_2$ emission. A large range of the visible spectrum was filtered in Dr. Lubinsky's tests to prevent the detection of 532 nm stimulation light as shown in Figure 26. Phosphorimetry analysis indicates that HoF_3 emits at 550 nm, which was filtered in these experiments. Selection of a longer excitation wavelength, so any PSL resulting from the 550 nm can be detected, would give insight into the HoF_3 contribution. Performing additional experiments with a high band pass filter which filters wavelengths less than 500 nm would be beneficial in determining the PSL due to $EuCl_2$.

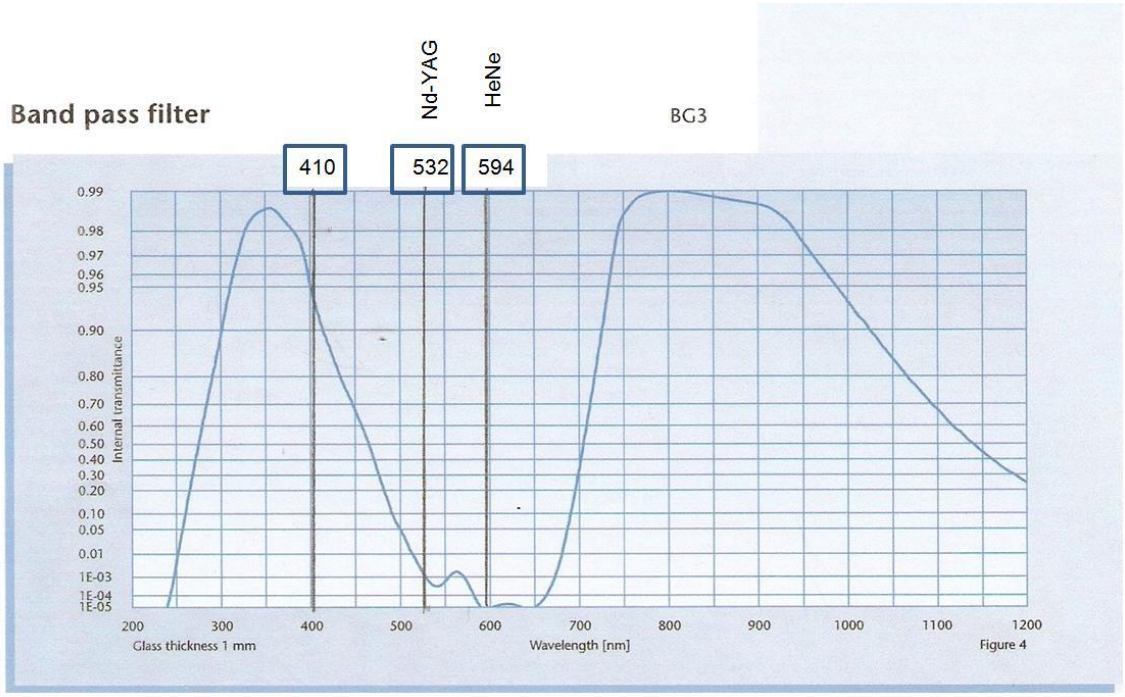

Figure 26. Schematic showing wavelengths of light that were filtered to prevent detection of the stimulation light

Mössbauer Spectroscopy

Mössbauer spectra were acquired for the sample prepared following temperature profile 1 (Figure 9) at 5K and 250K, temperature profile 2 (Figure 10) at 5K, 250K, and at 7K after being stored 165 days in a cooler at -80º C, and temperature profile 3 (Figure 11) at 6K and 143K. The fitted spectra are shown in Figures 27, 28, and 29. Site 1 (green) fits $EuCl_2$ and site 2 (blue) fits $EuCl_3$. The red line fits the entire spectrum which represents the superposition of the two site fits.

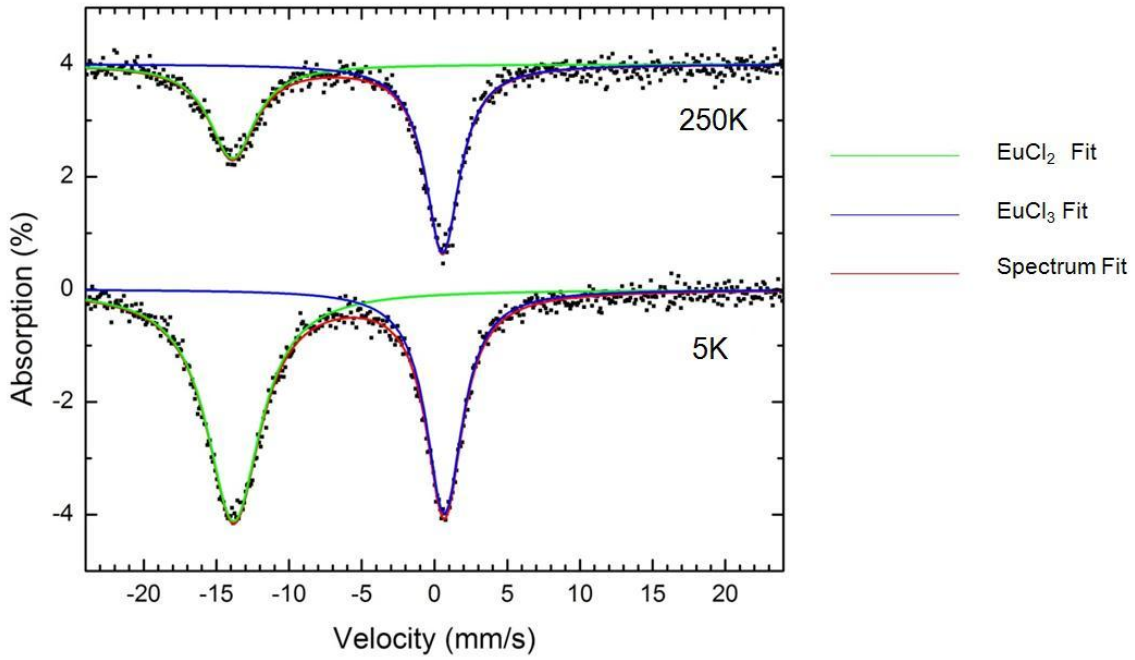

Figure 27. Fitted spectra for the sample prepared using Temperature Profile 1

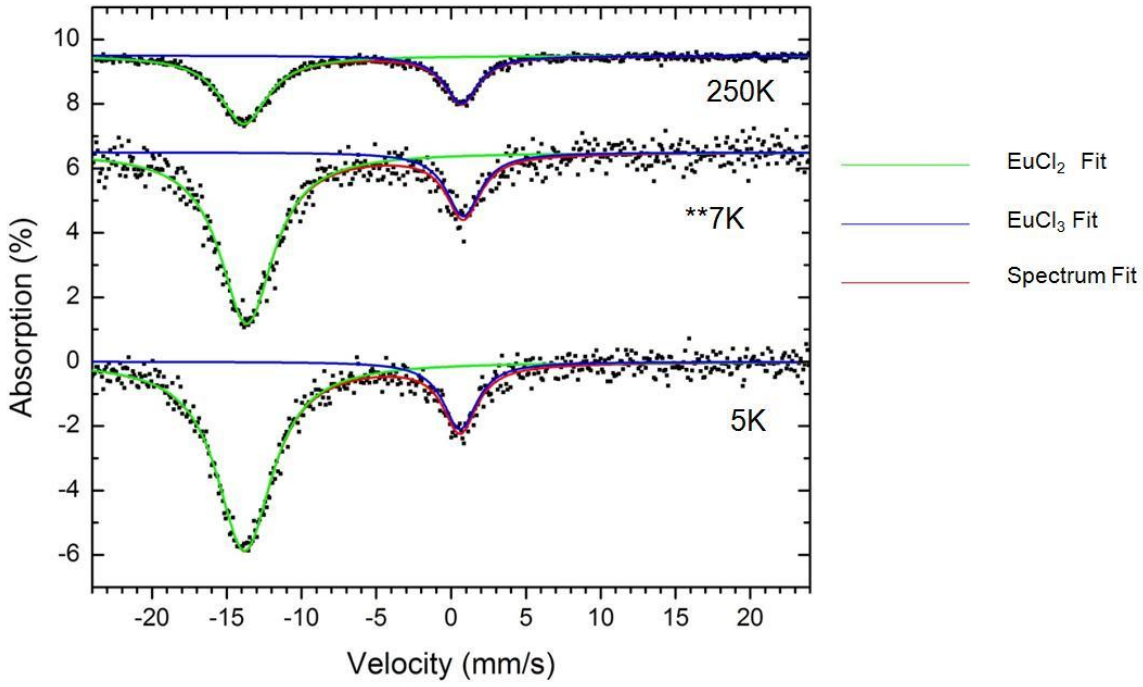

Figure 28. Fitted spectra for the sample prepared using Temperature Profile 2

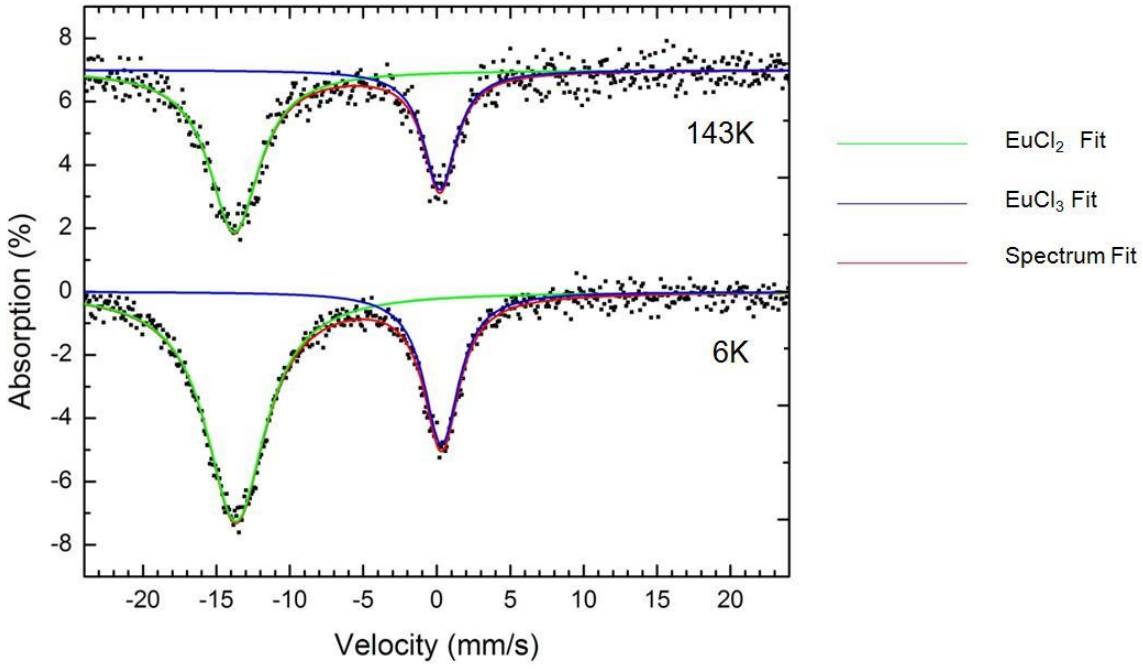

Figure 29. Fitted spectra for the sample prepared using Temperature Profile 3

The isomer/chemical shift provides information about the valence of atoms present in the sample. The entire spectrum is shifted in either the positive or negative direction depending upon the electron charge density of the s orbital. The s orbital overlaps the nucleus. The orbital is spherically symmetric and there is no angular momentum. The Mössbauer apparatus source is SmF_3 which decays to EuF_3. No isomeric shift would be seen for a EuF_3 sample since the absorber and source would be the same.

The chemical shift for the samples is listed in Table 6. Only a slight positive shift (0.35 - 0.86 mm/s) is seen in the spectra for Eu^{3+} site since the source is Eu^{3+}. This positive shift can be attributed to the fluorine source versus chlorine sample. The Eu^{3+} is the stable form of Europium. Eu^{2+} shifts to -14 mm/s relative to Eu^{3+}. The isomer shift for the Eu^{2+} ions ranges from -13.8 to -13.5. Temperature shifts are due to slower velocities at lower temperatures. The magnitude of the shift ranges from 0.08 to 0.19 mm/s.

Table 6. Isomer/Chemical Shift

Cryostat Temperature	Site 1 ($EuCl_2$) Isomer Shift	Site 2 ($EuCl_3$) Isomer Shift	Chi-Squared
Temperature Profile 1			
5K	-13.66	0.81	0.98
250K	-13.74	0.69	0.99
Temperature Profile 2			
5K	-13.66	0.74	0.94
7K (stored)	-13.61	0.86	1.02
250K	-13.80	0.72	0.97
Temperature Profile 3			
6K	-13.53	0.46	1.12
143K	-13.63	0.35	0.94

A chart showing line amplitudes and line widths is shown in Table 7. The broadened lines associated with Eu^{2+} are due to the relaxation of electron spin. Lines do not broaden during fast relaxation. This broadening is more discernible at lower temperatures. Line amplitudes become larger at lower temperatures. Lowering the temperature means the nucleus is more tightly bound in the solid.

At room temperature, the nucleus is not as tightly bound, and it becomes more difficult to differentiate between the Eu^{2+} and Eu^{3+} states.

Table 7. Line Amplitudes and Line Widths

Cryostat Temperature	Site 1 ($EuCl_2$) Line Amplitude	Site 1 ($EuCl_2$) Line Width	Site 2 ($EuCl_3$) Line Amplitude	Site 2 ($EuCl_3$) Line Width	Chi-Squared
Temperature Profile 1					
5K	0.0206	4.490	0.0199	3.016	0.98
250K	0.0084	3.846	0.0168	2.876	0.99
Temperature Profile 2					
5K	0.0293	4.532	0.0105	2.742	0.94
7K (stored)	0.0266	4.356	0.0099	2.790	1.02
250K	0.0106	3.899	0.0074	2.736	0.97
Temperature Profile 3					
6K	0.0363	4.929	0.0242	2.905	1.12
143K	0.0256	4.150	0.0189	2.707	0.94

The Mössbauer Effect is the probability of a gamma ray being absorbed and is equivalent to the area under the absorption curve (Figures 27, 28, & 29). The line broadening and greater amplitude height that occurs at lower temperatures increase the probability of detecting the Mössbauer Effect. Lower temperatures provide a truer representation of the percentage of the Eu^{2+} and Eu^{3+} present in each sample. Table 8 lists the relative percentage of Eu^{2+} and Eu^{3+} present in each sample.

Table 8. Relative Amounts of $EuCl_3$ and $EuCl_2$

Cryostat Temperature	Total Area (Mössbauer effect) (A.U.)	Site 1 ($EuCl_2$)		Site 2 ($EuCl_3$)	
		Area (A.U.)	Area%	Area (A.U.)	Area %
Temperature Profile 1					
5K	0.48	0.29	60.62 %	0.19	39.38 %
250K	0.25	0.10	40.11 %	0.15	59.89 %
Temperature Profile 2					
5K	0.51	0.42	82.16 %	0.09	17.84 %
7 K (stored)	0.45	0.36	80.70 %	0.09	19.30 %
250K	0.19	0.13	67.01 %	0.06	32.99 %
Temperature Profile 3					
6K	0.78	0.56	71.83 %	0.22	28.17 %
143K	0.49	0.33	67.50 %	0.16	32.50 %

The sample that was reduced using temperature profile 2 experienced the highest percentage of conversion to $EuCl_2$. More than 82% of the $EuCl_3$ was reduced to $EuCl_2$. After the initial measurements, the sample was stored in a coldbox at -80° C for 165 days and then re-tested on the Mössbauer apparatus. There was a slight decrease in the Mössbauer effect, suggesting that the sample may have undergone oxidation during storage. The sample reduced according to temperature profile 1 experienced 61% conversion and the sample reduced following temperature profile 3 had 72% conversion.

Each heating method decomposed a percentage of the $EuCl_3$. The reaction of the reduction is $EuCl_3 \rightarrow EuCl_2 + ½\ Cl_2$. The mass loss that occurred during the three thermal methods is shown in Table 9. The percentage of mass loss ranges from 12.3% to 23.6%. A sample experiencing 100% conversion would result in 13.7% mass loss. The additional mass loss must be attributed to some other mechanism than the intended reaction. This result is consistent with a 39.9% mass loss during a 10 minute thermal treatment of $EuCl_3$ reported in the literature. Distinct color changes ranging from gray to purple occurred during the heating process with all samples produced which is also consistent with the literature [25].

Table 9. Mass loss during reduction process

Temperature Profile	$EuCl_3$ Initial (grams)	$EuCl_3/EuCl_2$ Final (grams)	Mass Lost (grams)	Mass Loss (%) $(\frac{m_i - m_f}{m_i} x\ 100\%)$
(1)	0.0390	0.0298	0.0092	23.59
(2)	0.0306	0.0236	0.0070	22.88
(3)	1.3389	1.1739	0.1650	12.32

Sample size for the experiments following temperature profiles 1 and 2 are similar. Both experienced a large percentage of mass loss due to the unknown mechanism, but the sample prepared using temperature profile 2 experienced the highest conversion while the sample prepared using temperature profile 1 experienced the least conversion. Placing the sample in the furnace to undergo the ramp-up cycle proved detrimental to the overall conversion rate.

The reduction methods using temperature profiles 2 and 3 differed both in the time spent in the furnace (one vs. six hours) and in the sample size. The additional time spend in the furnace did not increase the conversion of $EuCl_3$ to $EuCl_2$. However, less mass loss occurred, suggesting that sample size is an important factor in the reduction procedure. The sample reduced using temperature profile 3 was 43 times larger than the sample reduced using temperature profile 2.

Possible causes for the additional mass loss include trace contaminants in the purchased $EuCl_3$ or interaction with the platinum crucible. The furnace was continually purged with argon during the reduction treatments, but the ceramic tube may leach a chemical which interacts with the samples.

Performing an experiment with a larger sample following temperature profile 2 would be beneficial in determining the influence of sample size. Additional experiments might also include varying the time samples spend in the oven to optimize the time required to achieve the greatest conversion.

CHAPTER 4

CONCLUSIONS

Co-doping FCZ glass with HoF_3 is a method of increasing conversion efficiency making it more suitable for CR imaging plates. HoF_3 singly doped FCZ does not exhibit any PSL at 532 nm stimulation. $EuCl_2$ appears to be a necessary component of FCZ if it is to be an efficient storage phosphor. $EuCl_2$ can be synthesized from $EuCl_3$.

Future work should include additional PSL experiments using a different stimulating wavelength so any HoF_3 emission can be detected. Additional FCZ samples co-doped with $HoCl_3$ should be prepared and tested to see how additional chlorines impact the PSL.

The $EuCl_3$ reduction experiment should be repeated using temperature profile 2 and a larger sample. Performing additional experiments varying the heating time could help optimize the process.

The viability of using synthesized $EuCl_2$ that has been reduced from $EuCl_3$ in FCZ glasses should be tested. One FCZ samples should be prepared using the synthesized dopant product from heat treatment and another FCZ sample prepared using purchased dopant chemicals. They should be characterized using DSC and heat treated to precipitate orthorhombic nanocrystals. Additional characterization (PL and XRD) should be performed to confirm and compare orthorhombic crystallization behavior in the two samples. Finally, PSL analysis should be performed to determine if this method of creating $EuCl_2$ is a feasible option as a dopant for storage phosphors.

REFERENCES

1. *Handbook of Medical Imaging*, ed. J. Beutel, H. Kundel, and R.V. Metter2000, Bellingham, Washington: SPIE Press.

2. Blasse, G. and B. Grabmaier, *Luminescent Materials*1994, New York, NY: Springer-Verlag.

3. Schweizer, S., et al., *Photostimulated luminescence in Eu-doped fluorochlorozirconate glass ceramics.*Applied Physics Letters, 2003.**83**(3): p. 449-541.

4. Johnson, J.A., S. Schweizer, and A. Lubinsky, *A Glass-Ceramic Plate for Mammography.* J. Am. Ceram. Soc., 2007.**90**(3): p. 693-698.

5. Chen, G., et al., *Fluorozirconate-based nanophase glass ceramics for high-resolution medical x-ray imaging.*Journal of Non-Crystalline Solids, 2006.**352**: p. 610-614.

6. Poulain, M., M. Poulain, and J. Lucas, *Verresfluores au tetrafluorure de zirconium proprieties optiques d'un verre dope au ND3+.*Materials Research Bulletin, 1974.**10**(4): p. 243-246.

7. Poulain, M. and A. Soufiane, *Fluoride Glasses: Synthesis and Properties.*Brazilian Journal of Physics 1992.**22**(3): p. 205-217.

8. Lecoq, A. and M. Poulain, *Fluoride glasses in the DrF4-Baf2-YF3-AlF3 Quaternary system.*Journal of Non-Crystalline Solids 1980.**41**: p. 209-217.

9. Choi, S. and G. Frischat, *Influence of crystallization on some properties of ZrF4_BaF2_YF3_AlF3 glasses.*Journal of Non-Crystalline Solids, 1991.**129**: p. 133-136.

10. Fedorov, V., A. Babitsyna, and T. Emel'yanova, *Glass Formation in the ZrF4-LaF3-BaF2-NaF System.*Glass Physics and Chemistry 2001.**27**(6): p. 512-519.

11. Zhu, X. and N. Peyghambarian, *High-Power ZBLAN Glass Fiber Lasers: Review and Prospect.*Advances in OptoElectronics, 2010.**2010**: p. 23.

12. Edgar, A., et al., *A new fluorozirconate glass-ceramic X-ray storage phosphor.*Journal of Non-Crystalline Solids, 2003.**326**: p. 489-493.

13. Johnson, J., et al., *Crystallization in heat-treated fluorochlorozirconate glasses.* Journal of Physics: Condensed Matter, 2009. **21**.

14. Paßlick, C., et al., *Structural properties of fluorozirconate-based glass ceramics doped with multivalent europium.* Journal of Applied Physics, 2011.**110**.

15. Chen, G., et al., *Insights into phase formation in fluorochlorozirconate glass-ceramic storage phosphors.* Applied Physics Letters, 2006.**88**(191915).

16. Paßlick, C., et al., *Differential scanning calorimetry investigations on Eu-doped fluorozirconate-based glass ceramics.* Journal of Non-Crystalline Solids, 2010.**356**: p. 3085-3089.

17. Henke, B., et al., *Erbium- and chlorine-doped fluorozirconate-based glasses for upconverted fluorescence.* Journal of Non-Crystalline Solids, 2009.**355**: p. 1916-1918.

18. Schweizer, S., et al., *Multi-functionality of fluorescent nanocrystals in glass ceramics.* Radiation Measurements, 2010.**45**: p. 485-489.

19. Pfau, C., et al., *Structural phase transitions of barium halide nanocrystals in fluorozirconate glasses studied by Raman spectroscopy.* Journal of Applied Physics 2011.**109**(8).

20. Pfau, C., et al., *Phonon spectra of barium halide nanocrystals in fluorozirconate glasses.* IOP Conf. Series: Materials Science and Engineering, 2010. **15**(012021).

21. Paßlick, C., et al., *Crystallization behavior of rare-earths doped FCZ glasses* Journal of Non-Crystalline Solids 2011. **357**: p. 2450-2452.

22. Schweizer, S., *Physics and Current Understanding of X-Ray Storage Phosphors.* Phys. Stat. Sol., 2001. **187**(2): p. 335-393.

23. Hendy, S. and A. Edgar, *Structure of fluorochlorozirconate glasses using molecular dynamics.* Journal of Non-Crystalline Solids, 2006.**352**: p. 415-422.

24. Pei, Z., et al., *Luminescence property of Eu-doped fluorochlorozirconate glass-ceramcs.* Journal of Rare Earths, 2009.**27**(2): p. 338-340.

25. Weber, J., et al., *The oxidation state of europium in halide glasses.* Journal of Physics: Condensed Matter, 2011. **23**.

26. Chen, W., *Process of Photoluminescence and Photostimulated Luminescence in BaFBr:Eu Phosphors.*Journal of Materials Science Technology, 1995.**11**(5): p. 388-390.

27. Henke, B., et al., *Eu oxidation state in fluorozirconate-based glass ceramics.*Journal of Applied Physics, 2009.**106**(113511).

28. Henke, B., et al., *XANES Studies of Eu-doped Fluorozirconarte Based Glass Ceramics.* MRS Proceedings, 2010. **1262**(1262-W08-03).

29. Librantz, A., et al., *Excited state dynamics of the Ho3+ ions in holmium singly doped and holmium, praseodymium-codoped fluoride glasses* Journal of Applied Physics, 2007. **101**(12): p. 123111.

30. Lahoz, F., et al., *Upconversion mechanisms in rare-earth doped glasses to improve the efficiency of silicon solar cells.* Solar Energy Materials and Solar Cells, 2011. **95**(7): p. 1671-1677.

31. Wnuk, A., et al., *Dynamics of the up-conversion emission in holmium doped ZBLAN fiber* RADIATION EFFECTS AND DEFECTS IN SOLIDS, 2003. **158**(1-6): p. 469-473.

32. da Vila, L., L. Gomes, and L. Tarelho, *Dynamics of Tm–Ho energy transfer and deactivation of the 3F4 low level of thulium in fluorozirconate glasses.*Journal of Applied Physics, 2004.**95**(10): p. 5451-5463.

33. Malinowski, M., et al., *Room temperature photon avalanche in Ho3+ doped YAF, YAP, YLF and ZBLAN.*Journal of Alloys and Compounds, 2001.**323**: p. 731-735.

34. Nishibu, S., S. Yonezawa, and M. Takashima, *Preparation and optical properties of HoF3-BaF4-AlF3_GeO2 glasses.*Journal of Non-Crystalline Solids, 2005.**351**: p. 1239-1245.

35. Leonard, R., et al., *Rare earth doped downshifting glass ceramics for photovoltaic applications.* (unpublished), 2012.

36. Kumar, G., et al., *Fluorescence and upconversion spectral studies of Ho3+ in alkali bismuth gallate glasses.*Journal of Alloys and Compounds, 2004.**365**: p. 117-120.

37. Schweizer, S. and J. Johnson, *Fluorozirconate-based glass ceramic X-ray detectors for digital radiography.*Radiation Measurements, 2007.**42**: p. 632-637.

APPENDICES

Appendix I

Input data reflects the PID controller temperature displayed, while the actual temperature represents the temperature inside the tube furnace near the sample.

Temperature program for Glass Synthesis

Prompt	Input Data	Actual		
C 01	25 °C	25 °C		Begin at Room Temperature
T 01	20 minutes	20 minutes		**********
C 02	427 °C	400 °C		20 minutes to ramp to 400 °C
T 02	60 minutes	60 minutes		**********
C 03	427 °C	400°C		60 minutes maintain at 400 °C
T 03	40 minutes	40 minutes		**********
C 04	825 °C	800 °C		40 minutes to ramp to 800 °C
T 04	60 minutes	60 minutes		**********
C 05	825 °C	800 °C		60 minutes maintain at 800 °C
T 05	45 minutes	45 minutes		**********
C 06	765 °C	750 °C		45 minutes to ramp to 750 °C
T 06	60 minutes	60 minutes		**********
C 07	765 °C	750 °C		60 minutes maintain at 750 °C
T 07	5 minutes	5 minutes		**********
C 08	725 °C	700 °C		5 minutes to ramp to 700 °C
T 08	5 minutes	5 minutes		**********
C 09	725 °C	700 °C		5 minutes maintain at 700 °C
T 09	60 minutes	60 minutes		**********
C 10	427 °C	400 °C		60 minutes to ramp to 400 °C
T 10	-121 minutes			Return to Room Temperature

Appendix II

Input data reflects the PID controller temperature displayed, while the actual temperature represents the temperature inside the tube furnace near the sample.

Temperature Program for Samples 1 & 2

Prompt	Input Data	Actual		
C 01	25 °C	25 °C		Begin at Room Temperature
T 01	20 minutes	20 minutes		**********
C 02	427 °C	400 °C		20 minutes to ramp to 427 °C
T 02	60 minutes	60 minutes		**********
C 03	427 °C	400°C		60 minutes maintain at 427 °C
T 03	40 minutes	40 minutes		**********
C 04	725 °C	700 °C		40 minutes to ramp to 725 °C
T 04	60 minutes	60 minutes		**********
C 05	725 °C	700 °C		60 minutes maintain at 725 °C
T 05	60 minutes	60 minutes		**********
C 06	427 °C	400 °C		60 minutes to ramp down to 427 °C
T 06	-121 minutes			Return to Room Temperature

Temperature Program for Sample 3

Prompt	Input Data	Actual		
C 01	25 °C	25 °C		Begin at Room Temperature
T 01	20 minutes	20 minutes		**********
C 02	427 °C	400 °C		20 minutes to ramp to 427 °C
T 02	60 minutes	60 minutes		**********
C 03	427 °C	400°C		60 minutes maintain at 427 °C
T 03	40 minutes	40 minutes		**********
C 04	725 °C	700 °C		40 minutes to ramp to 725 °C
T 04	360 minutes	360 minutes		**********
C 05	725 °C	700 °C		360 minutes maintain at 725 °C
T 05	60 minutes	60 minutes		**********
C 06	427 °C	400 °C		60 minutes to ramp down to 427 °C
T 06	-121 minutes			Return to Room Temperature

VITA

Sharon Kaye Gray was born in Richmond, Kentucky on March 13, 1954. She grew up near Eaton, Ohio and graduated from Eaton High School in 1972. After working in secretarial/clerical positions for 12 years, she left the workforce to devote time to family. During this time she was heavily involved in community volunteer activities. In 2004, while living in North Carolina, she enrolled in classes at Surry Community College, Dobson, NC. In 2005, she moved to Johnson City, Tennessee and attended East Tennessee State University. After graduation in 2009 from ETSU with a Bachelor of Science Degree in Physics, she worked briefly for Washington County, Tennessee. She returned to school at The University of Tennessee Space Institute in 2011 pursuing a Master's Degree in Biomedical Engineering with a biomaterials concentration.